

# MD simulation of indentation and scratching of single crystal aluminum

R. Komanduri<sup>\*</sup>, N. Chandrasekaran, L.M. Raff<sup>1</sup>

*Mechanical and Aerospace Engineering, Oklahoma State University, 218 Engineering North, Stillwater, OK 74078, USA*

Received 25 September 1998; received in revised form 15 February 2000; accepted 15 February 2000

---

## Abstract

Molecular Dynamics (MD) simulations of indentation and scratching have been conducted on single crystal aluminum in various crystal orientations and directions of scratching to investigate the anisotropy in hardness and friction. Depending on the crystal orientation, the atoms near the surface are found to be disturbed to different degrees due to repulsive forces between them as the indenter approaches the workmaterial. The hardness is found to increase significantly as the indentation depth is reduced to atomic dimensions. The calculated values of hardness are found to be an order of magnitude higher (and close to theoretical strength) than the corresponding engineering values which can be expected considering the size effect possible at indentation depths of a few nanometers or less. It thus appears that at very low depths of indentation (or nanoindentation), the plastic deformation underneath the indenter is governed by the theoretical yield strength of the material. The anisotropy in hardness and friction coefficient of single crystal aluminum with different crystal orientations and scratch directions is found to be in the range of 29%, which is close to the value of its anisotropy in the elastic range (21.9%) (stiffest in  $\langle 111 \rangle$  and least stiff in  $\langle 100 \rangle$ ) [R.W. Hertzberg, *Deformation and Fracture Mechanics of Engineering Materials*, 4th edn., Wiley, 1996, p. 14]. A similar observation was made in a recent investigation on the nanometric cutting of single crystal aluminum [R. Komanduri, N. Chandrasekaran, L.M. Raff, M.D. Simulation of Nanometric Cutting of Single Crystal Aluminum-Effect of Crystal Orientation and Direction of Cutting, 1998, accepted for publication in *Wear*]. Among the orientations investigated, hardness is maximum in (001)[100] and minimum in (012)[221]. Friction coefficient values are found to be higher (0.6–0.9) with the maximum along (001)[110] and minimum along (110)[110]. The [110] scratch direction represents the close packed direction for aluminum. The minimum and the maximum scratch hardness are observed with (111)[110] and (111)[211] crystal orientations. Although, similarities are found between nanoindentation and scratching, and nanometric cutting, the rake angle effect is found to be dominated by the large negative rake angle presented by the indenter in the former case. © 2000 Elsevier Science S.A. All rights reserved.

*Keywords:* Molecular Dynamics; Aluminum; Indention and scratching; Anisotropy

---

## 1. Introduction

Magnetic hard disks are used extensively in information storage systems. They are generally made of aluminum on which information is stored. The aluminum disks are invariably finished by ultraprecision machining. The stored information is protected from the read/write head (slider) by means of a thin coating (tungsten, nickel, etc.) in addition to a lubricant layer between the protective layer and the head. The coatings applied on the surface should have sufficient strength and wear resistance to withstand

the force applied by the slider. When the thickness is on the order of a few nanometers or less, even the slightest load can cause atomic rearrangement, which can result in the alteration of the mechanical and electrical properties. Hence, it is of paramount importance that the process should be investigated at the atomic level while performing low load, indentation and scratch experiments. The anisotropy of the workmaterial may play a significant role in the nature of plastic deformation, hardness and friction coefficient, etc. [1,2]. Significant research has been reported in the literature on the study of surface and bulk material properties using AFM and STM [3–5]. While such studies are essential, they can be somewhat expensive and time consuming. An alternate approach to this problem is Molecular Dynamics (MD) simulation in which high instrumentation costs are not a factor. This approach is the

---

<sup>\*</sup> Corresponding author. Fax: +1-405-744-7873.

E-mail address: ranga@ceat.okstate.edu (R. Komanduri).

<sup>1</sup> Chemistry Department.

subject of this investigation. In addition to its cost effectiveness, MD simulations permit a wide range of studies to be conducted. Examples include nanometric cutting, tribology, and nanomaterial testing.

Indentation and scratch tests have long been used to determine the hardness, the friction and wear characteristics, and the elastic properties of materials [6,7]. Hardness and friction coefficient are important properties when a slider moves on a substrate as in the case of disk drives and other nanotribological applications. The hardness test provides a means to measure the resistance to permanent or plastic deformation and the scratch test provides information regarding abrasion, friction coefficient, wear resistance, etc.

In general, in the hardness field, pyramidal indenters, such as Vicker's, Knoop, and various conical indenters are classified as "sharp" indenters while spherical indenters are labeled as "blunt" indenters. Also, indentation–scratch tests are generally conducted to simulate ultraprecision machining, grinding, or abrasion. Komanduri et al. [8,9] suggested the indentation–scratch model to be very appropriate particularly for ultraprecision machining with tools of large edge radius relative to depth of cut, or with large negative rake tools. It is interesting to note that the so-called "sharp" indenters, when applied to scratching or cutting, actually fall in the category of blunt tools as the rake angles are highly negative [8,9].

When the depth of indentation–scratching is in the range of nanometers (as in nanoindentation), indentation or scratching is performed within a single grain of a polycrystalline workmaterial as the average grain size is significantly larger (generally, several micrometers). Consequently, nanoindentation or scratching of a polycrystalline material basically involves machining a single grain with periodic interruptions at the grain boundaries. It is also known that the grain orientation changes slightly from one crystal to another in a polycrystalline aggregate. Hence, the indenter experiences workmaterial with different crystallographic orientations and scratch directions. In addition, there are many precision engineering applications where single crystal materials, such as silicon and germanium, are finished by nanometric cutting. The properties of these single crystal materials are determined by means of nanoindentation and sliding experiments.

Since some of the single crystal materials are anisotropic in their physical and mechanical properties, it is necessary to investigate their behavior in terms of crystallographic factors. Since the binding forces are strongly affected by the distance between the atoms in a crystal, the elastic constants in a single crystal will vary with the direction. For example, the modulus of elasticity in any direction of a cubic crystal is given by [10],

$$\frac{1}{E} = S_{11} - 2 \left[ (S_{11} - S_{12}) - \frac{1}{2} S_{44} \right] (l^2 m^2 + m^2 n^2 + l^2 n^2),$$

where the  $S_{ij}$  are the elastic constants in different orientations and  $l$ ,  $m$ , and  $n$  are the direction cosines. Consequently, properties, such as hardness, friction coefficient, etc. are highly influenced by the crystallographic factors.

Table 1 gives a summary of the elastic properties of polycrystalline aluminum as well as the stiffness, compliance constants, and elastic anisotropy of single crystal aluminum in different directions. It may be noted that aluminum has a degree of anisotropy of 1.219 in the elastic region (stiffest in  $\langle 111 \rangle$  and least stiff in  $\langle 100 \rangle$ ). In comparison, copper has a much higher degree of anisotropy of 3.203 [1]. It is possible to experience a somewhat similar anisotropy of these materials in the plastic range. For example, it is well known that for the FCC metals, slip is predominant on the  $\{111\}$  planes and  $\langle \bar{1}10 \rangle$  directions. In nanometric cutting, one would, therefore, expect these planes and directions to result in easy slip and perhaps lower cutting forces. It would be interesting to investigate the degree of anisotropy of aluminum in indentation–scratching and relate them with the anisotropy in the measured hardness and friction coefficient values.

With ever increasing demand for higher storage space and better performance, the surface finish is continuously being improved from nanolevels to atomic levels. Even though nano-instruments, which can apply extremely light loads (pico to micro Newtons) and perform hardness and scratch tests in the nanometer range have been developed, they still suffer from certain shortcomings. They include the need to conduct experiments in a highly controlled environment and significant costs involved in conducting the experiments in terms of time and effort. As the experimental range is pushed from macro–micro to nano-atomic levels, the degree of difficulty in performing these experiments increases significantly. While the integration of the computer with the testing systems is greatly facilitating this task, it can still be expensive. It is clear that analytical

Table 1

Summary of elastic properties of polycrystalline aluminum as well as the stiffness, compliance constants and elastic anisotropy of single crystal aluminum in different directions

Elastic modulus (GPa), polycrystalline	70.30
Shear Modulus (GPa), polycrystalline	26.1
Poisson's ratio, polycrystalline	0.345
Burger's vector	2.86
Relative degree of anisotropy *	1.219
$E_{111}$ (GPa)	76.1
$E_{100}$ (GPa)	63.7
$E_{110}$ (GPa)	72.59
$E_{111}/E_{100}$	1.19
$C_{11}$ ( $10^{10}$ Pa)	10.82
$C_{12}$ ( $10^{10}$ Pa)	6.13
$C_{44}$ ( $10^{10}$ Pa)	2.85
$S_{11}$ ( $10^{-11}$ Pa $^{-1}$ )	1.57
$S_{12}$ ( $10^{-11}$ Pa $^{-1}$ )	−0.57
$S_{44}$ ( $10^{-11}$ Pa $^{-1}$ )	3.51

\* $(2(S_{11} - S_{12}))/S_{44}$ .

methods based on continuum mechanics will not be appropriate for the analysis of the cutting process as the depth of cuts are reduced to nanometer range. In order to overcome the high costs, long testing times, degree of difficulty in the interpretation of the results, and technological constraints involved in conducting nanoscale experiments, modeling of the precision processes by MD simulation can be considered as a viable alternative in order to understand the process mechanics at the nanometric level. This is especially so when the MD simulation results complement the experimental results.

The objective of this study is to investigate the effect of crystallographic factors (crystal orientation and direction of scratching) in indentation and scratching of single crystal aluminum. MD simulations were conducted on single crystal aluminum along specific combinations of orientations  $\{(111), (110), (001), (\bar{1}20)\}$  and scratch directions  $\langle[\bar{1}10], [\bar{2}11], [100], [210], [221]\rangle$ . The nature of plastic deformation, dislocation generation, chip formation, extent of subsurface deformation, forces, force ratio, and specific energy with the crystallographic factors are examined in this investigation. The anisotropy in the indentation hardness, scratch hardness, and friction coefficient of aluminum single crystals with orientation effect is also investigated.

## 2. Literature review

### 2.1. Experimental studies of indentation and sliding process

While numerous studies have been reported on indentation, sliding, and the anisotropy in hardness and friction on a range of workmaterials [11–26], only a limited number of them were directed to aluminum and specifically on single crystal aluminum. In this investigation, since the focus of our study is on the latter, only the literature relevant to indentation and sliding of single crystal aluminum in different crystallographic orientations and direction of sliding are covered. The important conclusions of the studies on other materials are briefly summarized for completeness.

Petty [17] experimentally investigated the anisotropy in hardness of single crystal aluminum and its relation to the preferred orientation and earing using the Vicker's, Brinell, and Knoop indenters. As the anisotropy in hardness by a Vicker's pyramid or a Brinell ball could not be determined, a less symmetrical Knoop indenter was chosen. The  $\{100\}$ ,  $\{110\}$ , and  $\{111\}$  planes of aluminum were indented along different directions. The minimum and maximum hardness on the cube face were found to be along the  $\langle 110 \rangle$  and  $\langle 100 \rangle$  directions, respectively. The Knoop hardness on the  $\{110\}$  face of high-purity aluminum was reported to increase as the indenter direction moved from  $\langle 110 \rangle$  to  $\langle 100 \rangle$ . The hardness level on the  $\{110\}$  plane was found to be slightly higher than that of  $\{100\}$

plane. This was attributed to the increased resistance to compression offered by the  $\{110\}$  plane. However, it was also stated that this could be due to the differences in the purity of the samples. The  $\{111\}$  plane was reported to exhibit a lower degree of hardness variation with a minimum in the  $\langle 110 \rangle$  direction. Petty concluded that the form of variation of hardness with direction depended on the orientation of the surface, which can be related to the patterns in which the available slip systems intersected the surface and also to the interactions between the available slip systems.

Garfinckle and Garlick [18] conducted Knoop hardness tests on single crystal aluminum of different orientations  $\{(100), (110), \text{and } (210)\}$  and indentation directions  $(\langle 100 \rangle, \langle 110 \rangle, \langle 210 \rangle, \langle 211 \rangle, \langle 221 \rangle, \langle 421 \rangle)$ . They concluded that the hardness anisotropy was essentially dependent on the direction of the long axis of the indenter and not on the plane of indentation. The hardness values were found to be nearly the same for a given direction of indentation regardless of the plane of indentation. For example, on the  $\{100\}$ ,  $\{110\}$ , and  $\{210\}$  planes along the  $\langle 100 \rangle$  direction, they observed the hardness values to be 23.1, 22.6, and 22.1, respectively. Similar results were reported for other combinations of crystallographic orientation and direction of indentation. The maximum and the minimum hardness were reported to be in the  $\langle 100 \rangle$  and the  $\langle 111 \rangle$  directions, respectively. With the hardness reported as a function of the indentation direction alone, they suggested the possibility of predicting the hardness anisotropy of a crystal on a standard stereographic triangle.

Based on a number of studies on the anisotropy in hardness and friction of a range of workmaterials by various researchers [11–26], the following conclusions may be drawn.

- The anisotropy in hardness is an intrinsic property of all crystalline solids [11].
- The extent of anisotropy in hardness is determined essentially by the crystal structure and the primary slip systems which accommodate dislocation motion during indentation.
- The varying extent of work hardening associated with indentations does not appear to influence the anisotropy [12].
- An increase in strength with a decrease in the deformed area is generally observed. If the stressed volume is small enough that it lies between dislocations, a much higher strength might result.
- Dislocations can propagate in the indented area and hence, can account for the plastic deformation in the region of indentation [13].
- An increase in the hardness value with decreasing indentation depth [14] is observed.
- The dislocation density in the regions surrounding the indenter has an effect on the hardness [15]. An increase in the hardness occurs due to difficulty with which the dislocations are nucleated in the near surface region.

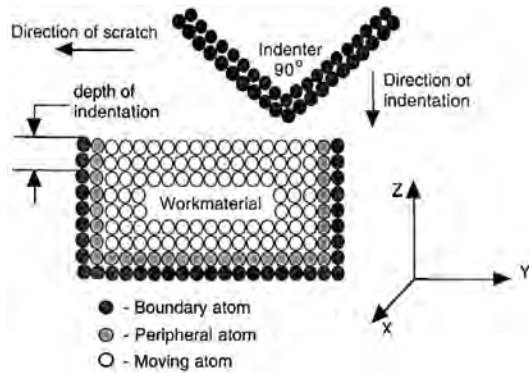


Fig. 1. Schematic of the indentation/sliding model used in the MD simulations showing various regions of interest, namely, the moving zone, the peripheral zone, and the boundary zone.

- Frictional anisotropy is reported to disappear below a critical load ( $\sim 0.1$  N), which is proportional to the square of the radius of curvature of the stylus, implying a critical contact pressure for Hertzian deformation [19].

- The plastic strain field after indentation is complicated and multiple slip systems have to be activated at the same time [6].

- High friction coefficients at low loads of 0.001 g [26] are observed. This is attributed to the surface energy of adhesion. These high values are in contrast to the results obtained using AFMs where the friction coefficients has been reported to be very low ( $10^{-2}$ – $10^{-3}$  range) when the loads applied are in the nanogram range.

Table 2

Computational parameters used in the MD simulation of nanometric cutting of aluminum single crystal

Configuration	3-D indentation–scratch	
Potential used (potential parameters for the workmaterial)	Morse potential ( $D_L = 0.2703$ eV, $\alpha_L = 1.1646/\text{\AA}$ , $r_{eL} = 3.253$ \AA and $r_c = 6.604$ \AA)	
Workmaterial dimension	$6a \times 25a \times 15a$ , $a$ -lattice constant	
Number of atoms in the workmaterial based on crystal set-up	Crystal set-up	No. of atoms
	(111) $[\bar{1}10]$	5131
	(111) $[\bar{2}11]$	5092
	(110) $[\bar{1}10]$	4550
	(110) [001]	4382
	(001) $[\bar{1}10]$	4998
	(001) [100]	4410
	(01 $\bar{2}$ ) [221]	4802
	( $\bar{1}20$ ) [210]	4940
Indenter dimension	$6a \times 15a \times 15a$ , $a$ -lattice constant 2551 total tool atoms	
Indenter material	Infinitely hard	
Indenter edge radius	Sharp edge	
Indenter rake angle	$-45^\circ$	
Indenter included angle	$90^\circ$	
Indentation/scratch depth	0.81 nm	
Width of scratch	2.12 nm	
Indentation/scratch speed	500 m/s	
Bulk temperature	293 K	

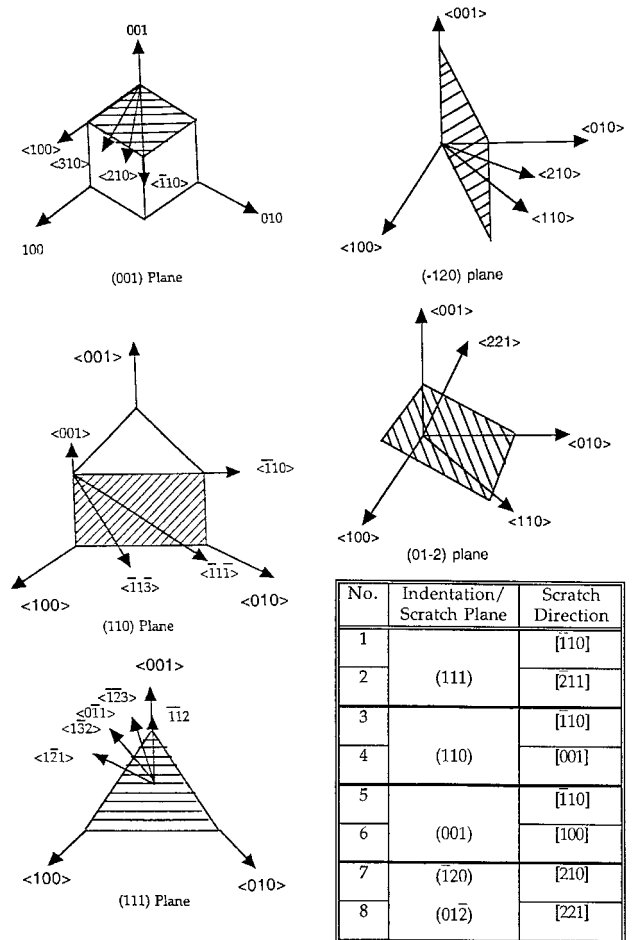


Fig. 2. Schematic showing various crystal orientations and the corresponding directions for cubic materials [2].

- Significantly higher values for friction force ( $10^{-6}$  N) are observed as the load tends to zero, which corresponds to a friction coefficient of infinity [20].

## 2.2. MD simulation of indentation and sliding process

MD simulation studies were initiated in the late 1950s at the Lawrence Radiation Laboratory (LRL) by Alder and Wainwright [27,28] in the field of equilibrium and non-equilibrium statistical mechanics. The application of MD simulation to cutting and indentation process was first introduced at Lawrence Livermore National Laboratory

Table 3

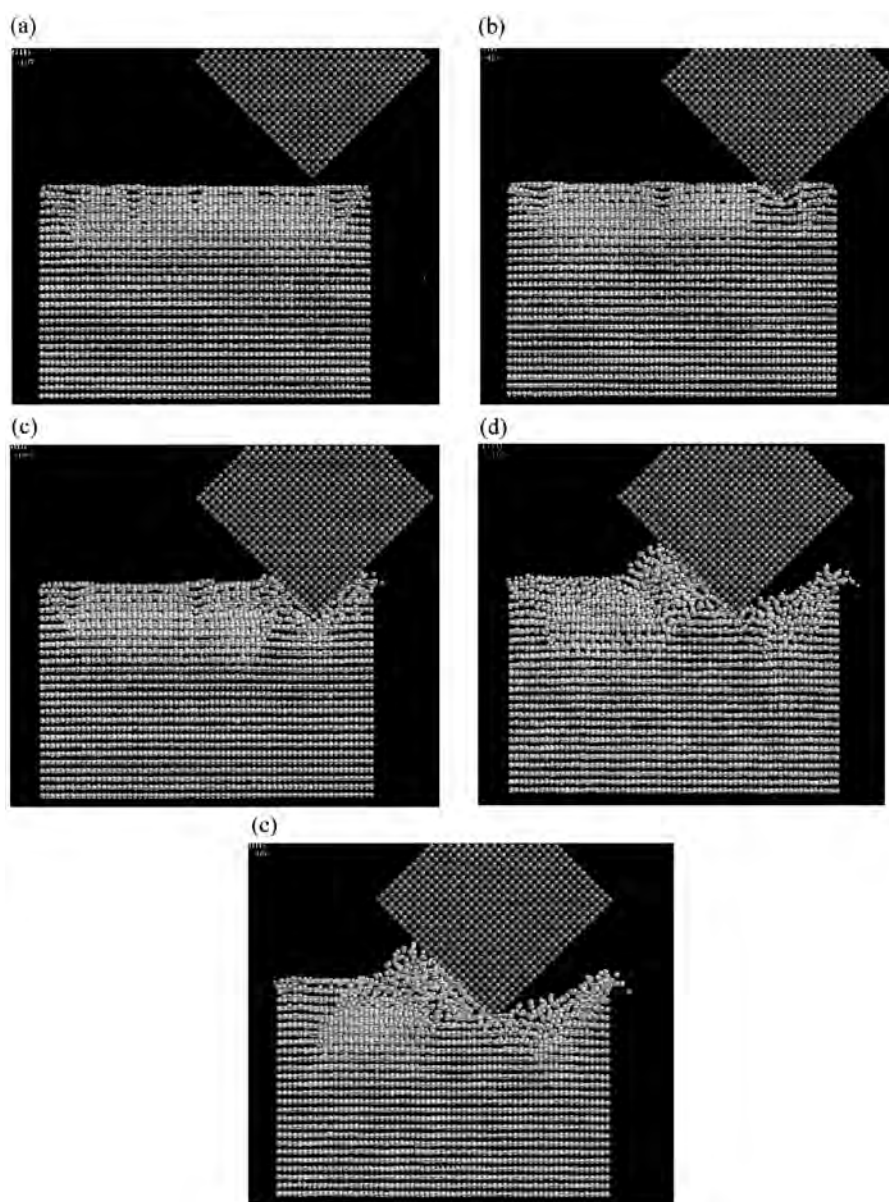
Atomic density and distance between planes for aluminum crystal (after Dieter [10])

Orientation	Atomic density per unit area ( $\text{\AA}^2$ )	Distance between planes ( $\text{\AA}$ )
Octahedral {111}	$4/\sqrt{3}a^2$ (0.141)	$a/\sqrt{3}$ (2.338)
Cube {100}	$2/a^2$ (0.122)	$a/2$ (2.025)
Dodecahedral {110}	$2/\sqrt{a^2}$ (0.086)	$a/2\sqrt{2}$ (1.432)

(LLNL) in the late 1980s and early 1990s [29–35]. Pioneering research in the field of MD simulation of indentation was conducted by Landman et al. [36–40] at Georgia Institute of Technology followed by Belak and his colleagues at the Lawrence Livermore National Laboratory (LLNL). Since then, MD simulation has been applied to a wide range of fields including crystal growth, low-pressure diamond synthesis, laser interactions, nanometric cutting [2,9,41–52], indentation [53–58], and tribology [59–63] to name a few. While some MD simulations of indentation [31,35–40,58] and sliding [59–63] studies have been reported in the literature, there are practically no investigations on the indentation and scratching of single crystal aluminum and in specific, the effect of crystallographic orientation. The principal materials for which indentation

and sliding that have been studied include Cu [35,58,60], Au [38,40], and Ag [35]. Therefore, in this section, we shall provide only a very brief review of a few examples of such theoretical investigations. MD simulations of the indentation process has been reported in great detail [36–40,53–58] as briefly summarized in the following. In the present investigation, the emphasis of the indentation studies is not on the details of the indentation process per se but to determine the anisotropy in hardness with crystal orientation.

Belak et al. [35] reported MD simulation of nanoindentation of copper and silver (111) surfaces with a blunt triangular diamond tip. However, an accurate potential for the diamond tip was not used. The velocities used in the simulations were 1, 10, and 100 m s<sup>-1</sup>. An initial van der



Figs. 3. (a)–(e) MD simulation plots showing various stages of the indentation–scratch test with the workmaterial set-up in the (111) $\bar{1}10$  orientation.

Waal's attraction followed by a linear increase in the load due to elastic response of the substrate was observed. The magnitude of the load was reported to be comparable to the experimental results in the literature using AFM's [64,65]. They reported the occurrence of a critical yielding phenomenon and a significant drop in the load after the tip had penetrated  $\sim 1.5$  layers into the substrate. Pile up of atoms around the tool tip was observed as the tool was indented further into the substrate ( $\sim 7$  layers). The substrate was reported to show elastic–plastic deformation. The cross-sectional plots through the tool tip showed the plastic deformation to be limited to a few lattice spacings surrounding the tip.

Landman and Luedtke [38,40] conducted MD simulations of indentation on a gold substrate using a nickel tool. A gradual increase in the force between the tip and the substrate was observed followed by a region of instability. This increase was interpreted as an increase in the attractive force between the tip and the substrate. They noted that the gold atoms under the tip were displaced by  $\sim 0.2$  nm towards the tool tip. Jump-to-contact (JC) was reported at a tip to substrate separation distance of 0.42 nm and this was accompanied by an increase in the attractive force.

Yan and Komvopoulos [58] conducted MD simulations to analyze the deformation occurring during indentation of a dynamic substrate by a single atom or hard tip. They also studied the effects of substrate temperature and indentation speed on the force, deformation behavior, and energy dissipation. In their study of the single atom indentation process, they used both argon and copper as the substrates when a hard tip was used. They reported a hysteresis in the normal force versus separation distance curve for both cases (atom or rigid tip as indenter) studied. The direction of irreversible deformation coincided with the macroscopic plastic flow. They observed the material differences to exhibit a strong influence on the force–distance curve.

Buldum and Ciraci [60] conducted MD simulation of nanoindentation and sliding of a nickel tip on a copper substrate. Specifically, they conducted tests with a sharp nickel (111) tool on copper (110) surface and a blunt nickel (001) tip on copper (001) surface. An Embedded atom potential was used to simulate the metallic bonds of nickel and copper. In the case of a sharp tool, movement of atoms from the tool tip towards voids in the substrate at a separation distance of 0.43 nm was reported. The forces were reported to be almost negligible at large separation distances and increased with decreasing separation distance between the tool tip and the workmaterial. They also reported the phenomenon of JC to take place as the tip was lowered into the substrate. When the tool was pulled away from the substrate, stretching of the junction formed by the indenter and consequent neck formation were reported. Contrary to the sharp tool, the JC was reported to initiate from the softer material (substrate) when a blunt tip was used in the simulations. Multiple JCs were observed when a sharp tip was used, in contrast to the single JC using a

blunt tip. A quasi periodic variation in the force was reported during sliding of the sharp nickel tip on the copper substrate. This was attributed to the stick-slip process involving phase transitions.

MD simulations of friction between surfaces were reported by Kim and Suh [61] based on the assumption that the plowing component of friction is the dominant factor contributing to friction. This assumption was based on the earlier experimental results of Suh and Saka [22]. The simulation was performed for a single atom scanning across the surface of a 2-D Lennard Jones type crystal in both static and dynamic modes. Normal force was kept very low to avoid mechanical interactions, such as plowing, asperity deformation, etc. The interfacial interaction was strictly repulsive. In the case of static simulations, a periodic oscillation of the tangential force and the normal force as the atom scans the lattice was reported. The friction coefficient was observed to oscillate between  $-0.8$  and  $0.8$  for a case when the scan height was  $1.1a$ , where  $a$  is the lattice parameter of the surface.

Eventhough, significant research has been reported in the literature on the mechanics of indentation–sliding process at nanometric level, a number of problems still remain. In many of the indentation studies, it is implicitly assumed that there is chemical interaction between the indenter and the workmaterial, while most practical indentation tests are conducted with a tool that is chemically incompatible with the workmaterial. It thus appears that in the modeling of the indentation, the tool should be considered as infinitely rigid with no interaction between the indenter and the workmaterial. This can simulate many of the hardness tests with cemented tungsten carbide and diamond indenters when indenting a range of workmaterials. It is, also, not clear whether hardness anisotropy depends on the plane of indentation, or direction of indentation, or a combination. Also, friction coefficient values ranging from 0.05 [61] to infinity [20] have been reported in the literature. It should also be noted that the experi-

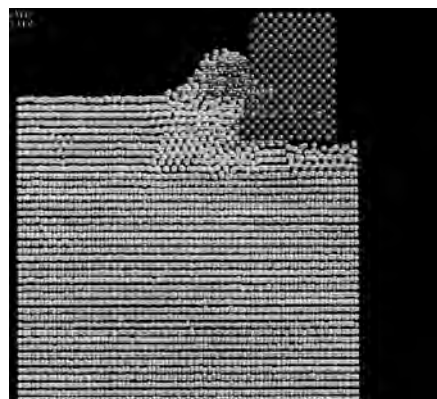
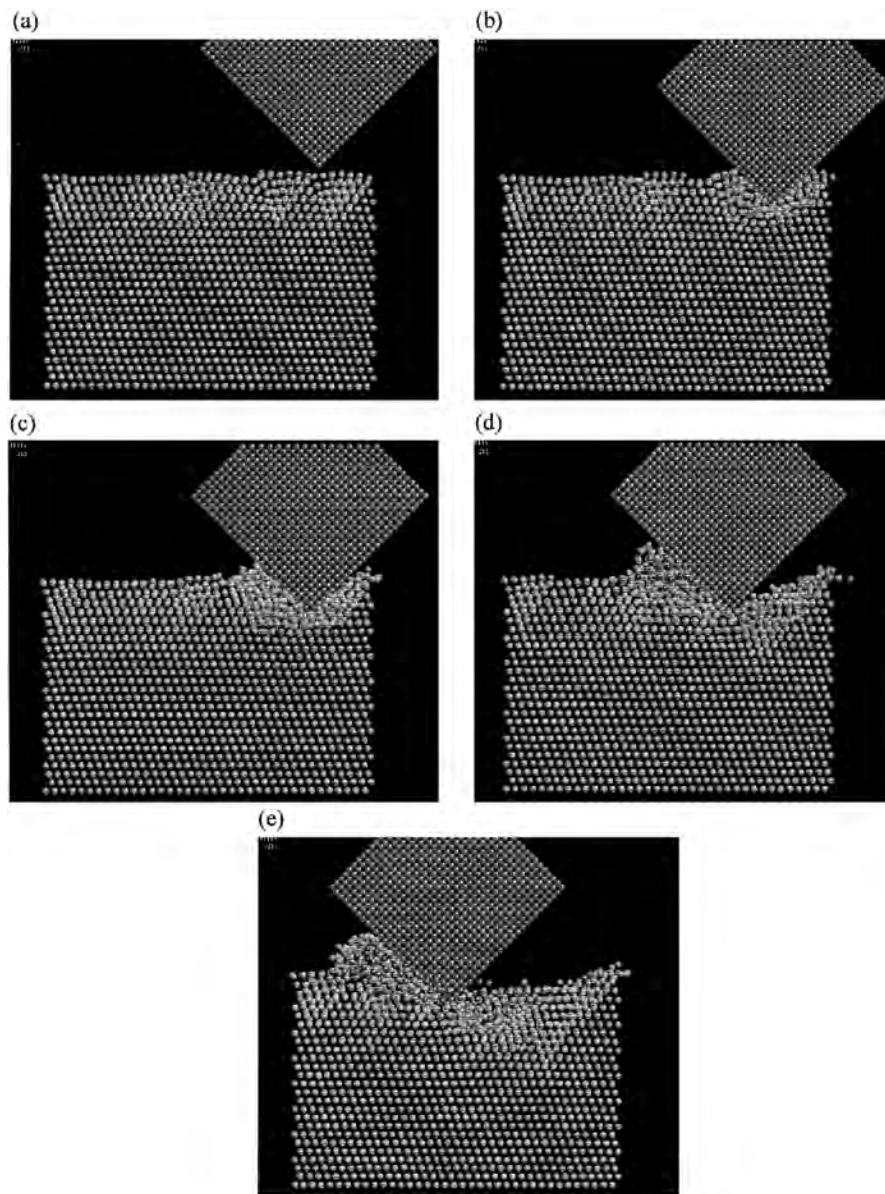


Fig. 4. MD simulation of nanometric cutting of single crystal aluminum with the (111)[ $\bar{1}10$ ] orientation showing dislocations generated parallel to the cutting direction [2].

ments reported in the literature relating to the effect of anisotropy are performed at the micrometer level [11–26]. Also, in nanosliding/nanoscratching, what may be relevant is the value of the friction force at light loads rather than the coefficient of friction. As the latter is merely the ratio of the two forces, namely, the scratch force to the normal force, the numerical value of the ratio can be high even though the values of the individual forces can be extremely low [63]. Based on earlier studies on grinding [66] and machining with high negative rake tools [9,67], this ratio may be more influenced by the geometry of indenter.

It would be of great interest to extend this problem to the nanometric-atomic level for many nanotribological ap-

plications. The effect of anisotropy on hardness and friction coefficient has not yet been attempted at the atomic level, as previous MD studies of indentation–sliding did not specifically address this problem. The effect of crystallographic orientation and direction of scratching on the friction coefficient are also not well understood. In this investigation, an MD simulation approach was used to investigate the effect of crystallographic factors on indentation and scratching of single crystal aluminum. The variation of the indentation and scratching process mechanics with crystallographic factors are discussed in some detail. The effect of crystallographic factors is also discussed in terms of anisotropy in hardness, friction coefficient, forces, force ratio, and specific energy.



Figs. 5. (a)–(e) MD simulation plots showing various stages of the indentation–scratch test with the workmaterial set-up in the  $(111)[\bar{2}11]$  orientation.

### 3. Methodology for MD simulation of indentation and scratch tests

#### 3.1. Indentation and scratch model

Fig. 1 is a schematic of the model used in the MD simulation studies on the effect of crystallographic factors in indentation and scratch tests of single crystal aluminum. The workmaterial is divided into three different zones, namely, the moving zone (P-zone), the peripheral zone (Q-zone), and the boundary zone (B-zone) [68]. The motion of the atoms in the moving zone is determined solely by the forces produced by the interaction potential and the direct solution of classical Hamiltonian equations of motion. The motions of the peripheral atoms are also calculated from the solution of Hamiltonian equations, but modified by the presence of velocity reset functions associated with each atom in the peripheral zone. In this method, the Cartesian velocity components of each peripheral lattice atoms is reset at periodic time intervals, using the following algorithm:

$$v_{\alpha i}^{\text{new}} = (1 - w)^{1/2} v_{\alpha i}^{\text{old}} + w^{1/2} V(T, \xi),$$

where  $v_{\alpha i}^{\text{old}}$  is the  $\alpha$ -component ( $\alpha = x, y, \text{ or } z$ ) of velocity of lattice atom  $i$  resulting from the solution of the Hamiltonian equations of motion and  $v_{\alpha i}^{\text{new}}$  is the reset  $\alpha$  velocity component.  $w$  is a parameter that controls the strength of the reset with  $w = 0$  corresponding to a no reset and  $w = 1$  to a complete reset.  $V(T, \xi)$  is a randomly chosen velocity from a Maxwell–Boltzmann distribution at temperature  $T$ .  $\xi$  is a random number whose distribution is uniform in the interval  $[0,1]$  that controls the random selection. This procedure simulates the thermostatic effect of the bulk and guarantees that the equilibrium temperature will approach the desired value, which is 293 K in these calculations. More details relating to this thermostating method are given in Chandrasekaran et al. [51] and in the original paper by Riley et al. [68]. The boundary atoms are fixed in position and serve to reduce the edge effects and maintain the proper symmetry of the lattice.

#### 3.2. MD simulation conditions

MD simulations of indentation and scratching were conducted on single crystals of aluminum using a Digital  $\alpha$ -workstation (Model 500) with a clock speed of 433 MHz to study the effect of crystallographic factors, namely, crystal orientation, and indentation and scratch directions. Indentation and scratching were conducted along specific combinations of the orientation of the work material  $\{(111), (110), (001), \text{ and } (\bar{1}20)\}$  and scratch direction  $\langle [\bar{1}10], [\bar{2}11], [100], [210], \text{ and } [221] \rangle$  at a speed of  $500 \text{ m s}^{-1}$ . The indentation/scratch depth was maintained constant at 0.81 nm in all simulations. The specific combinations for the (111)  $z$ -axis are the  $y$  directions  $[\bar{1}10]$  and  $[\bar{2}11]$ , for the

(110)  $z$ -axis are the  $y$  directions  $[\bar{1}10]$  and  $[001]$ , for the (001)  $z$ -axis are the  $y$  directions  $[\bar{1}10]$  and  $[100]$ , and for the  $(\bar{1}20)$   $z$ -axis the  $y$  direction is  $[210]$  and for the  $(01\bar{2})$   $z$ -axis the  $y$ -direction being  $[221]$ , respectively. In the following discussion, the crystal set-up is referred to as  $(z)\langle y \rangle$ . For example,  $(001)\langle 100 \rangle$  represents the crystal being set-up with (001) as the  $z$ -axis and  $\langle 100 \rangle$  as the  $y$ -axis. The planes perpendicular to the  $z$  and the  $y$  axes have the same Miller indices. For example, the plane perpendicular to  $\langle 100 \rangle$  direction will be (100). The indentation is performed along the  $z$ -axis and the scratch is performed along the  $y$ -axis. For convenience, an infinitely hard (nickel) tool was used in these simulations as tool wear is hardly a problem in the nanoindentation of aluminum.

It may be noted that nanoindentation experiments are performed at much slower rates ( $10^{-6}$  to  $10^{-9}$  m/s), but if conducted at these rates, MD simulations would take extremely long processing times even with the fastest microprocessors. Currently, this is one of the drawbacks of MD simulations. It is possible that the large tool speeds may produce spurious effects. It is also possible that the properties that we are investigating can be insensitive to tool speed so that no physical effects are produced. Since we cannot execute the MD simulations at experimental speeds of  $10^{-6}$  to  $10^{-9}$  m/s, these theoretical methods cannot be used to investigate this point. However, it is possible to study indentation, scratching, and cutting at tool speeds in the experimental range using Monte Carlo simulation techniques. At present, we are developing computer codes to implement such studies. We anticipate that comparison of Monte Carlo results with MD simulations will provide a clear picture of the artifacts, if any, that are generated by employing high tool speeds.

Table 2 gives the computational parameters, details of the workmaterial and tool dimensions, indentation depth, and length of scratch used in the simulations. Fig. 2 shows the various crystal orientations and the corresponding di-

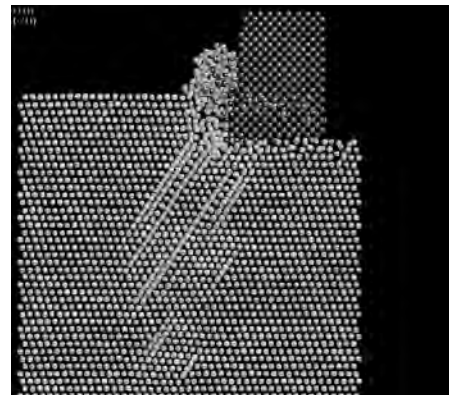
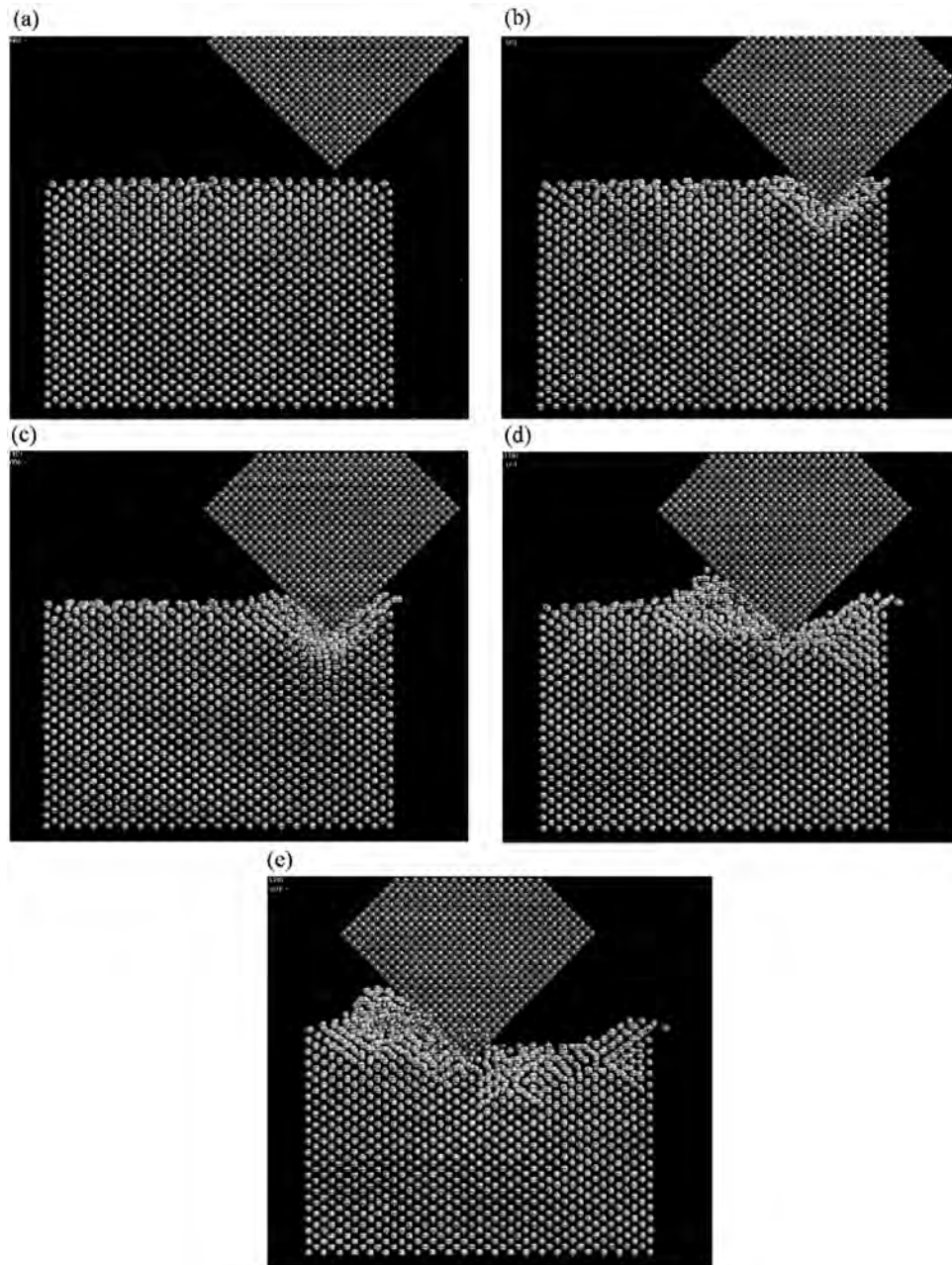


Fig. 6. MD simulation of nanometric cutting of single crystal aluminum with the  $(111)\langle \bar{2}11 \rangle$  orientation showing dislocations generated  $\sim 60^\circ$  to the cutting direction [2].



Figs. 7. (a)–(e) MD simulation plots showing various stages of the indentation–scratch test with the workmaterial set-up in the (110)[001] orientation.

rections for cubic materials. The total number of atoms in the workmaterial ranges from 4382 to 5131 depending on the crystal set-up while the tool has 2551 total atoms. It should be noted that while the simulation size of the workmaterial is maintained constant (Table 2) the number of planes and consequently, the total number of atoms considered in the simulation size depend on the crystal orientation. Consequently, the indentation–scratch width will change with orientation and scratch direction. While, the workmaterial orientation is varied, the tool orientation is maintained constant in all the simulations (Table 2).

Table 2 also tabulates the total number of atoms in the workmaterial for various combinations of crystal orientation and cutting direction.

The potential used in the simulations is a pairwise sum of Morse potentials between the lattice atoms of the workmaterial plus a second summation of pairwise Morse potentials between the atoms of the tool and those in the workmaterial, i.e.

$$V_{\text{total}} = V_{\text{T}} = \sum_{i=1}^{N_{\text{w}}} \sum_{j>i}^{N_{\text{w}}} V_{\text{M}}^{\text{L}}(r_{ij}) + \sum_{i=1}^{N_{\text{w}}} \sum_{j=1}^{N_{\text{T}}} V_{\text{M}}^{\text{TL}}(r_{ij}),$$

where  $r_{ij}$  is the  $i$ - $j$  interparticle distance and

$$V_M^L(r_{ij}) = D_L \left[ \exp\{-2\alpha_L(r_{ij} - r_{eL})\} - 2\exp\{-\alpha_L(r_{ij} - r_{eL})\} \right] \quad \text{for } r_{ij} \leq r_c,$$

$$V_M^L(r_{ij}) = 0 \quad \text{for } r_{ij} > r_c,$$

$$V_M^{TL}(r_{ij}) = D_T \left[ \exp\{-2\alpha_T(r_{ij} - r_{eT})\} - 2\exp\{-\alpha_T(r_{ij} - r_{eT})\} \right] \quad \text{for } r_{ij} \leq r_c,$$

$$V_M^{TL}(r_{ij}) = 0 \quad \text{for } r_{ij} > r_c.$$

$N_W$  and  $N_T$  are the number of lattice atoms in the workmaterial and tool, respectively. The potential parameters for the workmaterial,  $D_L$ ,  $\alpha_L$ , and  $r_{eL}$  are adjusted to the measured sublimation enthalpy, Debye temperature, and nearest-neighbor spacings for aluminum. The three parameters for the tool-workmaterial potential,  $D_T$ ,  $\alpha_T$ , and  $r_{eT}$  are obtained by standard combining rules with the parameters for the pure materials. The cutoff radius ( $r_c$ ) is chosen such that the ratio of the potential at the cutoff point to that at equilibrium is less than 4%. The use of such a cutoff radius ensures that the calculations will not consume large quantities of computational time in evaluating the forces that are near zero. It should be noted that there are no potential terms connecting the atoms of the tool with the workmaterial atoms in the boundary zone. Consequently, the tool can, in effect, move through the B-zone atoms as if they are not present. The potential parameters for the workmaterial are given in Table 2.

The MD simulations require the solution of  $6N$  ( $N$  — total number of atoms) simultaneous, coupled, first-order differential equations of motion. This solution is obtained using a fourth-order Runge–Kutta algorithm with a fixed integration step size of 0.1 atomic time unit. Integration accuracy is monitored using back-integration and energy conservation requirements with the velocity reset procedure turned off.

The use of pairwise potential in the simulation merits some comment. Numerous trajectory investigations of complex chemical reactions in the gas phase [69] and in the solid state under matrix isolation conditions [70] have shown that pairwise potentials yield accurate results so long as the process under investigation does not involve the scission and formation of covalent chemical bonds. If the machining process involves covalently bonded materials, such as silicon or diamond, more complex potential forms must be employed. Other potential forms can, of course, be used for any system. One such potential is the embedded-atom potential. Further MD studies will employ this formulation for the potential. When these calculations are complete, a comparison of the present results obtained with pairwise potentials with those given by an embedded-atom functional form will permit an accurate assessment of the sensitivity of the computed dynamics to the pairwise assumption.

Table 3 gives the atomic density and the distance between planes with respect to orientation of the aluminum crystal [10]. In the case of aluminum, an FCC material, the atomic density is maximum for the (111) plane and minimum for the (110) plane. Similarly, the distance between the atoms in a given direction of sliding is also important in the consideration of slip, for slip will occur on the densest planes and the shortest directions. Thus, a combination of both these factors affect the nature of plastic deformation of this material in nanoindentation–scratching.

It may be noted that width of the indenter was kept the same as the width of the workmaterial and the tool center coincided with the workmaterial origin during indentation–sliding. Even though, in practice, the indenter’s width is smaller than the workmaterial width, this approach is adapted here for a better visualization of the deformation process during MD simulation, which will not be the case when the width of the indenter is smaller than the workmaterial. In that respect, the indenter has a 2-D geometry. The semi-included angle of the indenter was  $45^\circ$ . This corresponds to a  $-45^\circ$  negative rake angle of the indenter during the scratch process. It is known that indenter geometry will affect the nature of deformation during indentation and scratching and it is hoped that the results of the MD simulations of indenters of different included angles will be published soon.

## 4. Results and discussion

### 4.1. M.D. simulation results

In the following, results of MD simulation of the indentation–scratch process on single crystal aluminum in different orientations and scratch directions are presented to investigate the process dependence on crystallographic factors. It may be noted that the description of the process is

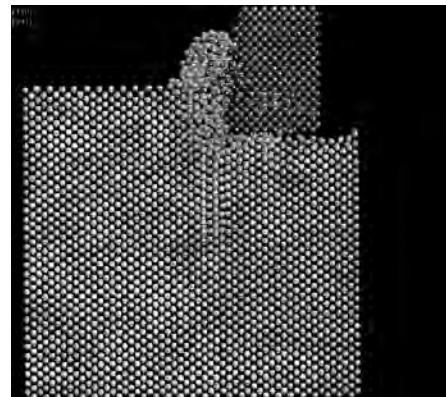


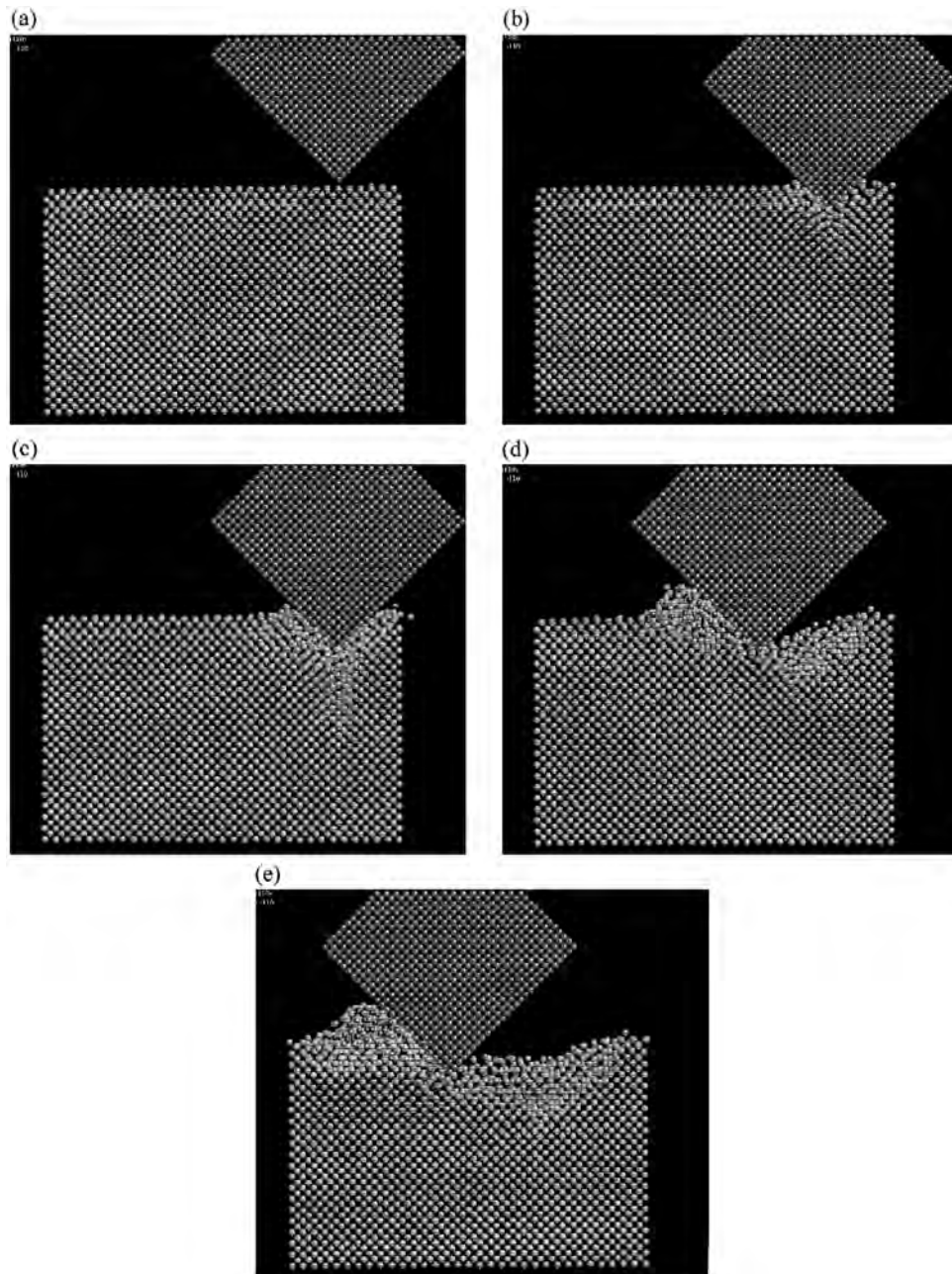
Fig. 8. MD simulation of nanometric cutting of single crystal aluminum with the (110)[001] orientation showing dislocations generating perpendicular to the cutting direction both below and above the workmaterial in the shear zone [2].

based not only on the simulation plots but also on the detailed animation studies of the MD simulation process. Since, the scratching process is somewhat similar to cutting, they will be compared where appropriate.

It may be noted that the width of the workmaterial used in the nanometric cutting studies reported earlier [2] was four lattice spacings compared to six lattice spacings in the present study. Consequently, some of the process phenomenon, such as the generation and propagation of dislocations was easier to delineate when the width was narrower, since in the animation pictures all the layers of atoms are superimposed. The width of the workmaterial in

the current study was increased to six lattice spacing to simulate 3-D conditions more closely. It may also be noted that even though some of the observations were observed more clearly in nanometric cutting [2] than in the present study, the essential features, such as deformation ahead of the tool and dislocation propagation direction with respect to the scratch direction remained the same.

Figs. 3(a)–(e) shows various stages of the MD simulation of the indentation–scratching process with the workmaterial–indenter set up in the  $(111)[\bar{1}10]$  combination. Fig. 3(a) shows a zone of disturbed material ( $\sim 8$  layers) from the surface (covering the entire length) extending into



Figs. 9. (a)–(e) MD simulation plots showing various stages of the indentation–scratch test with the workmaterial set-up in the  $(110)[\bar{1}10]$  orientation.

the workmaterial in the form of an inverted trapezium prior to contact with the indenter. Prior to this, the atoms were found to be in the relaxed condition. The trapezium is symmetrically located with respect to the workmaterial eventhough the indenter is approaching at one end. It is also not clear what role the boundary atoms play in truncating the sides of the trapezium. In addition, some voids or missing atoms can also be seen. These are attributed to the initial attractive forces followed by high repulsive forces experienced by the workmaterial atoms as the indenter approaches the workmaterial surface. As will be shown shortly, the zone of disturbed (shape and size) material prior to contact by the indenter on the workmaterial was found to vary with the orientation. The maximum was observed along the  $(111)\bar{1}10$  orientation. Animation of the indenter approaching the workmaterial showed compression of the top layers of the workmaterial as a result of an increase in the forces as the work-indenter separation distance was decreased. Fig. 3(b) shows indentation into the workmaterial and the displacement of some atoms from the workmaterial towards the surface. The pile up is higher on the right of the indenter due to placement of the boundary atoms closer to the indentation site on that side. The wide zone of disturbed material, which was present prior to indentation into the workmaterial was no longer present during the indentation process under the indenter. The length of the trapezium on the surface is reduced and is determined by the contact point of the indenter at the surface. Fig. 3(c) shows the indenter at the maximum indentation depth and just prior to the initiation of the scratch process showing a small region of plastically deformed material directly underneath the indenter. In addition, slip along the sides of the indenter can also be seen.

Fig. 3(d) is an intermediate stage of the scratch process showing displacement or pile-up of material ahead of the indenter in the form of a chip similar to machining with a high negative rake angle (here, the indenter presents a rake angle of  $-45^\circ$ ) or plowing. Animation of the scratching process showed slip to take place on layers of material parallel to the scratch direction ahead of the indenter (within the scratch depth). Slip of layers parallel to the cutting direction was also observed in nanometric cutting with a  $10^\circ$  rake tool [2]. In this study, compression ahead of the indenter to a greater extent can be observed from Fig. 3(e). It may be noted that the  $(111)\bar{1}10$  combination involves the most dense plane with scratching performed along the close packed direction (Table 3). Komanduri et al. [2] also reported the deformation ahead of the tool to be compression combined with shear along the cutting direction with the  $(111)\bar{1}10$  orientation (Fig. 4). The degree of compression ahead of the tool in nanometric cutting (Fig. 4) is less in comparison to the current study (Fig. 3(e)). This in part is attributed to the differences in the tool rake angle. The final stage of the scratch process (Fig. 3(e)) shows considerable amount of subsurface deformation, estimated to be equal to the indentation–scratch depth.

From an earlier study for a  $10^\circ$  rake tool [2] the subsurface deformation for similar conditions was observed to be much lower. This suggests that with increase in the negative rake, the extent of subsurface deformation increases [9,52]. Some elastic recovery of the workmaterial following the indentation–scratch process can also be seen from Fig. 3(e) and the animation of the process. The material removal process during scratching is predominantly plowing due to high negative rake angle of the indenter.

Figs. 5(a)–(e) show various stages of the MD simulation of the indentation–scratching process with the workmaterial set-up in the  $(111)\bar{2}11$  orientation. Fig. 5(a) shows the initial disturbance in the form of trigons (in the shape of inverted triangles with each triangle slightly separated from each other) near the surface of the workmaterial prior to contact with the indenter. However, the extent of this disturbance is less in comparison to the  $(111)\bar{1}10$  orientation (Fig. 3(a)) indicating differences in the forces experienced by the workmaterial prior to contact by the indenter. Fig. 5(b) shows the plastic deformation to be concentrated around as well as the sides of the indenter. Fig. 5(c) shows the indenter at the maximum indentation depth (0.81 nm) and just prior to the initiation of the scratch process. The deformation around the indenter as well as the region of deformation appears to be quite extensive (compare Figs. 3(c) and 5(c)). Also, the trigon under the indenter is no longer prominent due to extensive plastic deformation (Fig. 5(c)). The amount of pile-up of the workmaterial seems to be higher in this case compared to the earlier orientation (compare Figs. 3(c) and 5(c)).

Fig. 5(d) is an intermediate stage of the scratch process showing displacement or pile-up of material ahead of the indenter in the form of a chip similar to machining with a high negative rake angle ( $-45^\circ$ ). The deformation in the chip in the form of slip appears to take place predominantly parallel to the tool face (Fig. 5(e)). In nanometric cutting [2] for a similar crystal orientation with a  $10^\circ$  rake tool (Fig. 6), the material in the shear zone was observed to deform at an angle of  $\sim 60^\circ$ . In the present investiga-

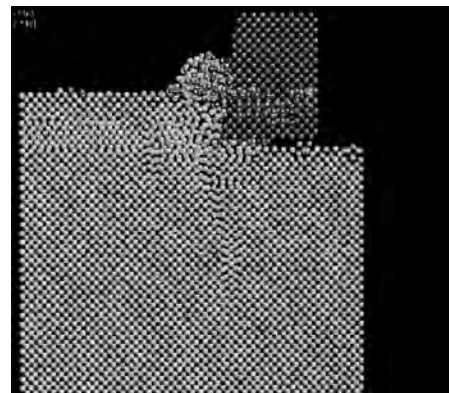
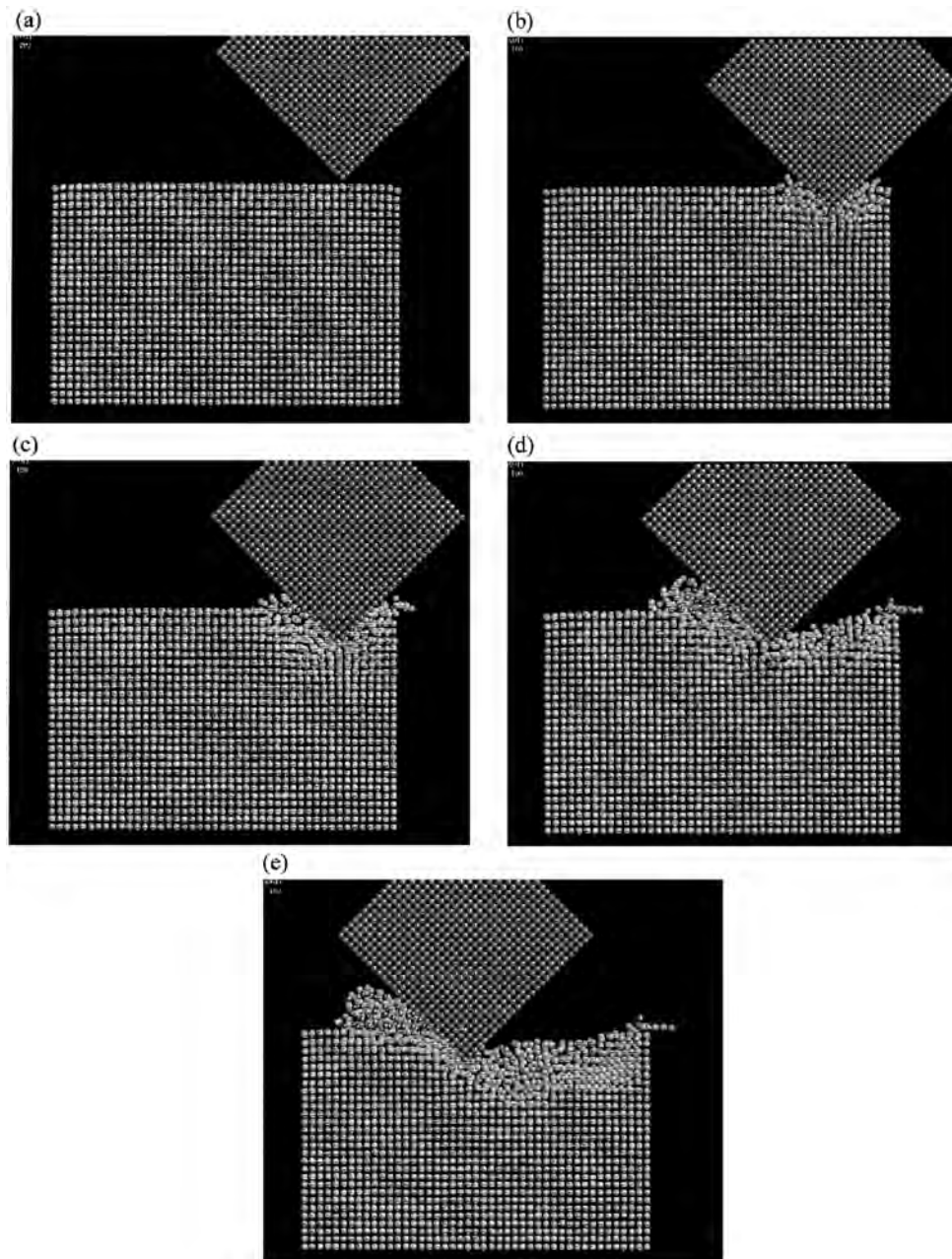


Fig. 10. MD simulation of nanometric cutting of single crystal aluminum with the  $(110)\bar{1}10$  orientation showing dislocations generating both parallel and perpendicular to the cutting direction [2].

tion, due to large negative rake angle of the indenter ( $-45^\circ$ ), the direction of slip seems to be controlled somewhat by the tool rake face. Also, in the nanometric cutting study [2], dislocations were found to be generated at  $\sim 60^\circ$  to the cutting direction in the workmaterial (Fig. 6). Even though, in the current study, such extensive dislocations at  $\sim 60^\circ$  are not clearly visible from Fig. 5(d), the animations showed the generation of dislocations in the same direction. One can see their presence in Fig. 5(e) in the machined surface after the indenter had advanced during scratching. Incidentally, the two sides of the inverted trigons observed prior to indentation were also formed at

$60^\circ$  to the scratch direction. Comparison of Figs. 3(e) and 5(e) indicates higher elastic recovery with the  $(111)\bar{2}11$  orientation than  $(111)\bar{1}10$ . The subsurface deformation and the chip volume appears to be lower with the  $(111)\bar{2}11$  orientation compared to  $(111)\bar{1}10$  (Fig. 3(e)). Similar results were reported in the previous study of nanometric cutting with a  $10^\circ$  rake tool [2].

Figs. 7(a)–(e) shows various stages of the MD simulation of the indentation–scratching process with the workmaterial–indenter setup in the  $(110)[001]$  combination. Fig. 7(a) shows practically negligible initial disturbance on the top layers of the workmaterial. Animation studies of



Figs. 11. (a)–(e) MD simulation plots showing various stages of the indentation–scratch test with the workmaterial set-up in the  $(001)[100]$  orientation.

the indentation process indicated that what little disturbance that was present was distributed uniformly. Fig. 7(b) and (c) are two stages of indentation. They (along with the animation studies) show dislocations generating underneath the tip of the indenter in the direction of indentation and moving towards the free surface of the workmaterial. A similar observation was made in nanometric cutting with a  $10^\circ$  rake tool with the dislocations generating both below and above the workmaterial in the shear zone (Fig. 8) [2]. Significant differences in the shape of the deformation region in the work material due to indentation can be observed depending on the crystal orientation (compare (Figs. 3(c), 5(c), and 7(c))). It was also reported that this mode of deformation was unique as no such mode was observed in conventional machining. In the scratch process, because of the large negative rake of the indenter, the deformation of the material was found to occur nearly parallel to the indenter face (Figs. 7(d) and (e)). This suggests that the geometry of the tool can strongly affect the mode of dislocation generation and propagation even though the crystal orientation is the same. Fig. 7(e) also indicates that the chip volume and subsurface deformation to be slightly lower than the other two cases discussed thus far (Figs. 3(e) and 5(e)).

Figs. 9(a)–(e) shows various stages of the MD simulation of the indentation–scratching process performed with the workmaterial–indenter set up in the  $(110)[\bar{1}10]$  combination. Fig. 9(a) shows practically negligible disturbance in the workmaterial prior to the contact of the indenter. Fig. 9(b) shows the amount of initial deformation and around the indenter to be minimal. Indentation on the crystal with  $(110)[\bar{1}10]$  combination generated dislocations both parallel and perpendicular to the indentation direction although the former were more obvious (Fig. 9(c)). A similar observation was made in the MD simulation of nanometric cutting for a similar orientation (Fig. 10) [2]. This is attributed to the fact that  $\langle 110 \rangle$  is the easy slip direction and when either indented or machined along that direction will generate dislocations along  $\langle 110 \rangle$  direction. Cross slip from the indenter’s tip towards the free surface and into the workmaterial can be observed from Fig. 9(c). As the indenter moved along the  $[\bar{1}10]$  direction the dislocations generated underneath the tool tend to disappear due to elastic recovery (Fig. 9(d)).

Comparison of Figs. 7(d) and 9(d) suggests a higher degree of plastic deformation ahead of the tool with the  $(110)[001]$  combination. However, in the previous study [2],  $(110)[\bar{1}10]$  crystal set-up was observed to show higher degree of plastic deformation ahead of the tool in contrast to the current observation. The degree of elastic recovery seems to be higher with the current crystal set-up. Fig. 9(e) shows the final stage of the indentation–scratch process. The elastic recovery can be observed to be higher than that experienced with  $(111)[\bar{1}10]$  combination (Fig. 3(e)) However, the chip volume is lower than  $(111)[\bar{1}10]$  (Fig. 3(e)) and  $(111)[\bar{2}11]$  (Fig. 5(e)) and seems to be nearly equal to

that of  $(110)[001]$  orientation (Fig. 7(e)). The subsurface deformation can be estimated to be nearly equal to the scratch depth (Fig. 9(e)).

Figs. 11(a)–(e) show various stages of the MD simulation of the indentation–scratching process performed with the  $(001)[100]$  orientation. Negligible disturbance in the work material prior to the contact of the indenter was observed (Fig. 11(a)). No visible dislocation pattern was observed during the initial stages of the indentation process. Initiation of dislocations at  $\sim 45^\circ$  into the workmaterial was observed during the animation (at maximum depth) followed by rapid elastic recovery. Consequently, as soon as the scratch process commences, the dislocations were observed to rearrange or escape towards the free surface. Fig. 11(c) shows the final stage of the indentation process wherein the workmaterial is largely undisturbed except for the region around the indenter. Fig. 11(c) shows displacement of atoms towards the free surface of the workmaterial by the indenter. Fig. 11(d) is an intermediate stage of the scratch process along  $[100]$  direction showing the material removal taking place as in conventional machining with the generation of a chip via the shear zone. However, the dislocations propagating at  $\sim 45^\circ$  into the workmaterial and  $\sim 45^\circ$  in the shear zone which was clearly observed in the nanometric study (Fig. 12) [2] was not observed during the scratch process. The final stage of the scratch process (Fig. 11(e)) shows that the deformation ahead of the indenter in the scratch process is rather limited.

Figs. 13(a)–(e) shows various stages of the MD simulation of the indentation–scratching process performed with the workmaterial–indenter set up in the  $(001)[\bar{1}10]$  combination. Fig. 13(a) shows that only the top layer is disturbed prior to the indenter’s contact with the workmaterial. Fig. 13(b) shows the progress of indentation. It is interesting to note dislocations propagating along the  $[\bar{1}10]$  direction which is perpendicular to the direction of indentation even before the commencement of the scratch process. This is

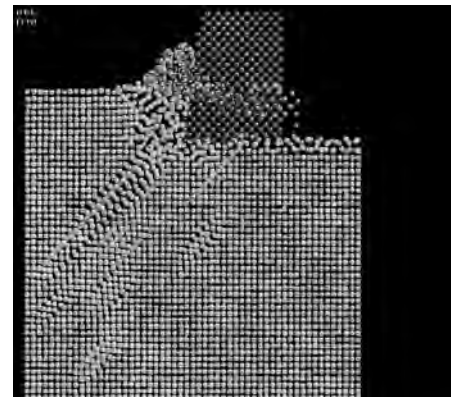
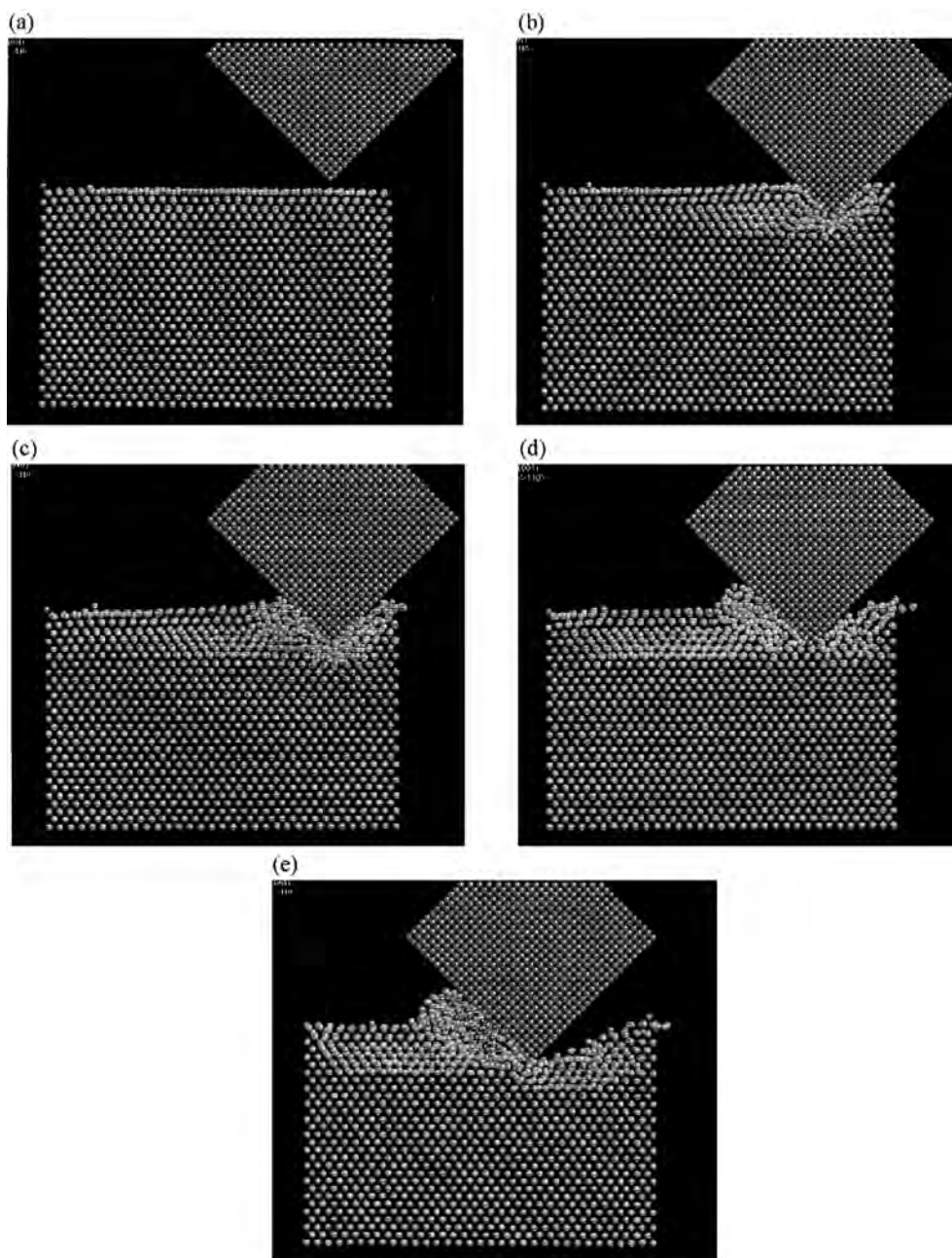


Fig. 12. MD simulation of nanometric cutting of single crystal aluminum with the  $(001)[100]$  orientation showing dislocations generated  $\sim 45^\circ$  to the cutting direction both in the work material and a mirror image in the shear zone [2].

found to be unique to this particular combination of crystal set-up. Dislocations propagating parallel to the cutting direction ( $[\bar{1}10]$ ) were also observed in nanometric cutting for similar crystal combination  $((001)[\bar{1}10])$  in an earlier study on nanometric cutting (Fig. 14) [2]. As scratching progresses (Fig. 13(d) and (e)) the number of dislocations propagating along the scratch direction was observed to increase. This is due to the fact that  $[\bar{1}10]$  is the close packed direction for the FCC crystal set-up and consequently slip is predominant when scratching along  $[\bar{1}10]$  direction. In the nanometric study [2], additional dislocations moving parallel to the cutting direction even below

the depth of cut was observed (Fig. 14). Similar observation can be made for indentation–scratching as shown in Fig. 13(e).

Figs. 15(a)–(e) show various stages of the MD simulation of the indentation–scratching process with the workmaterial–indenter set up in the  $(120)[210]$  combination. Fig. 15(a) shows minimal disturbance of the top layer of the workmaterial prior to the indenter's contact with the workmaterial. Figs. 15(b) and (c) show the deformation to be limited to the region around the indenter. Fig. 15(d) and (e) shows two stages during the scratch process. Slip seems to take place along the  $[210]$  direction although



Figs. 13. (a)–(e) MD simulation plots showing various stages of the indentation–scratch test with the workmaterial set-up in the  $(001)[\bar{1}10]$  orientation.

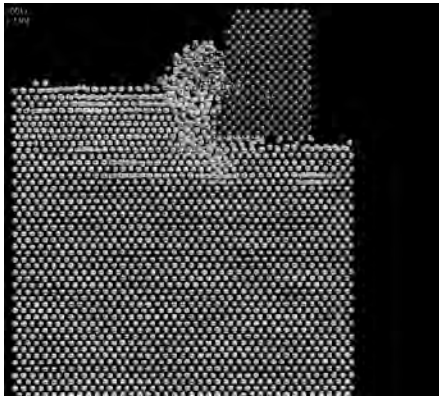


Fig. 14. MD simulation of nanometric cutting of single crystal aluminum with the  $(001)[\bar{1}10]$  orientation showing dislocations generating parallel and to the cutting direction [2].

modified by the large negative rake angle presented by the indenter as the indenter moves during the scratch process. Plastic deformation is limited to a small region ahead of the tool. The chip volume seems to be nominal. The subsurface deformation is seen to extend to  $\sim 3\text{--}4$  layers beneath the scratch depth.

Figs. 16(a)–(e) show various stages of the MD simulation of the indentation–scratching process with the workmaterial set up in the  $(01\bar{2})[221]$  combination. Some initial disturbance of the top layers of the workmaterial prior to the indenter's contact with the workmaterial was observed (Fig. 16(a)). Figs. 16(a) and (b) show two stages of indentation. The deformation is seen to concentrate near the indenter. Figs. 16(d) and (e) show intermediate and final stages of the scratch process showing deformation in the shear zone taking place parallel to the indenter face. It may be noted that this orientation resulted in minimum forces.

In Figs. 3–16, the generation and propagation of dislocations can be seen contrary to some of the experimental work where no dislocations were reported for indentation depths of less than 50 nm [15]. During indentation, dislocations were observed to propagate both parallel and perpendicular to the indentation direction in the case of  $(110)[\bar{1}10]$  combination. Dislocations propagating parallel to the indentation direction are observed in the case of  $(001)[\bar{1}10]$  combination. Some of these dislocations have been found to escape towards the free surface or rearrange themselves to proper crystal symmetry due to elastic recovery as the indenter was removed from the workmaterial or moved away from the indent during scratching. The amount of plastic deformation during indentation was observed to be maximum on (111) plane with different directions of indentation investigated. The pile up of the workmaterial around the tool was observed to be maximum in the case of  $(111)[\bar{2}11]$  combination. During sliding, the elastic recovery was observed to be minimum for the case of  $(001)[\bar{1}10]$  combination and maximum for the  $(111)[\bar{2}11]$  combination. The subsurface deformation towards the end

of the sliding process was observed to be maximum for the case of (111) and the directions of sliding considered with subsurface deformation along  $[\bar{1}10]$  scratch direction slightly higher than that of  $[\bar{2}11]$ . The minimum subsurface deformation was observed in the case of  $(001)[\bar{1}10]$  and  $(001)[100]$  orientations. The chip volume at the end of the scratch process was observed to be maximum for the case of  $(111)[\bar{1}10]$  combination and minimum in the case of  $(\bar{1}20)[210]$  combination. The dislocations do facilitate in the initiation of the plastic deformation as seen above in addition to the vacancies as mentioned by Belak et al. [35] (observed during the animation process). The presence of vacancies supplement the hypothesis presented by Belak et al. [35] that plasticity in the case of small scale indentation is likely to be due to the creation and movement of point defects.

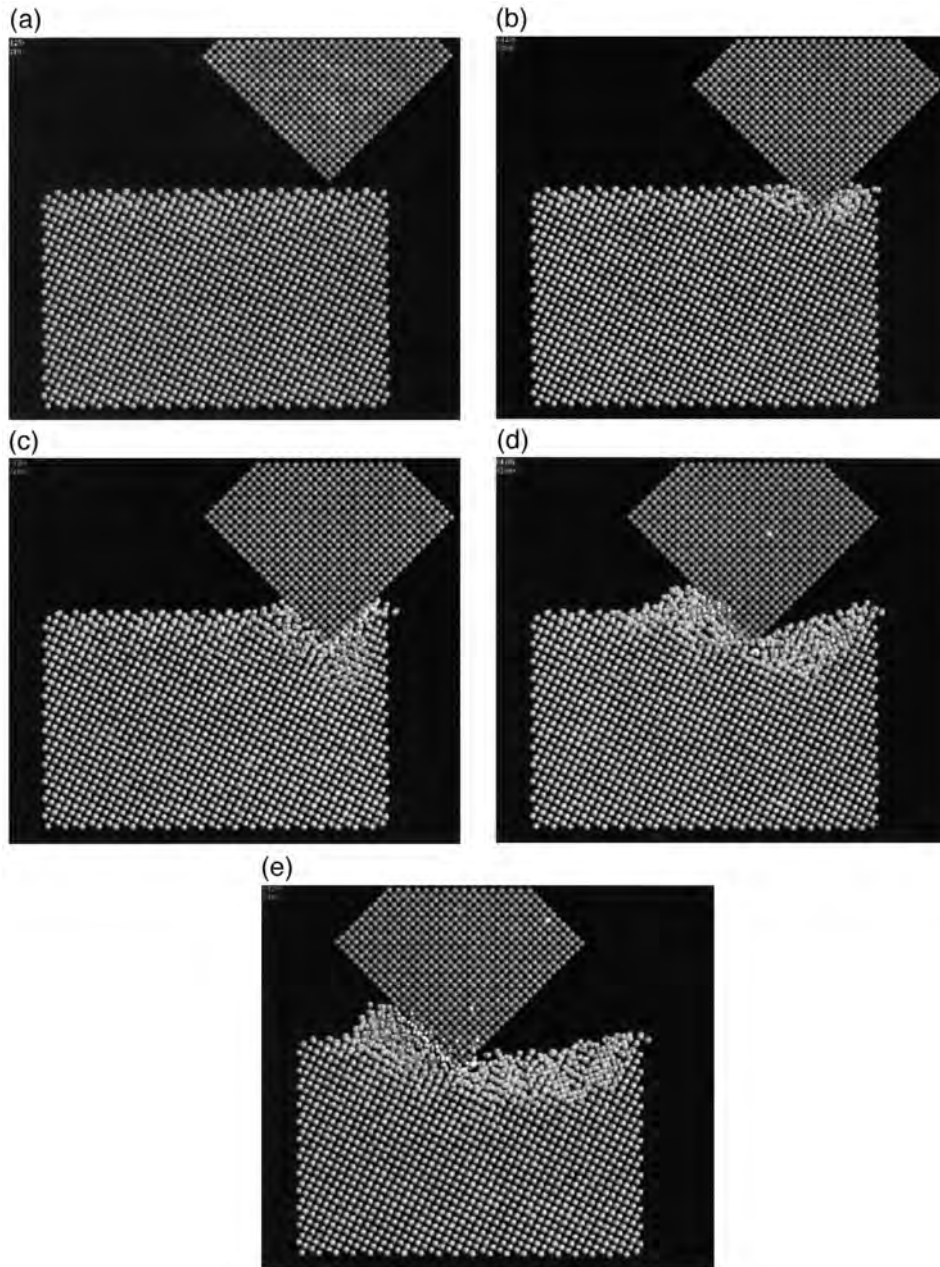
#### 4.2. On the nature of variation of the forces prior to indentation

A comparison of Figs. 3(a)–16(a) shows that the disturbance of the workmaterial prior to indenter's nominal contact to be maximum in the case of  $(111)[\bar{1}10]$  and  $(111)[\bar{2}11]$  combinations, and then by  $(110)[001]$  and  $(001)[\bar{1}10]$  combinations. Insignificant or practically no disturbance was observed for the other combinations, namely,  $((110)[\bar{1}10]$ ,  $(001)[100]$ ,  $(01\bar{2})[221]$ , and  $(\bar{1}20)[210]$ ) studied. Since the response of the workmaterial atoms prior to indenter's contact is different for different crystal set-ups, the corresponding forces prior to indenter's contact should also exhibit similar differences. In order to study this phenomenon, force data was collected during the initial stages of indentation prior to indenter's contact with the workmaterial. The forces in the MD simulations are evaluated from the first derivative of the potential equation. That is,

$$\text{Force: } F_{x_i} = - \frac{\partial V_i}{\partial X_i} = \dot{P}_{x_i},$$

where  $V$  is the potential of the body, and  $X = [x, y, z]$ . The forces in the  $z$  and  $y$  directions (Fig. 1) represent the normal and tangential (scratch) force components.

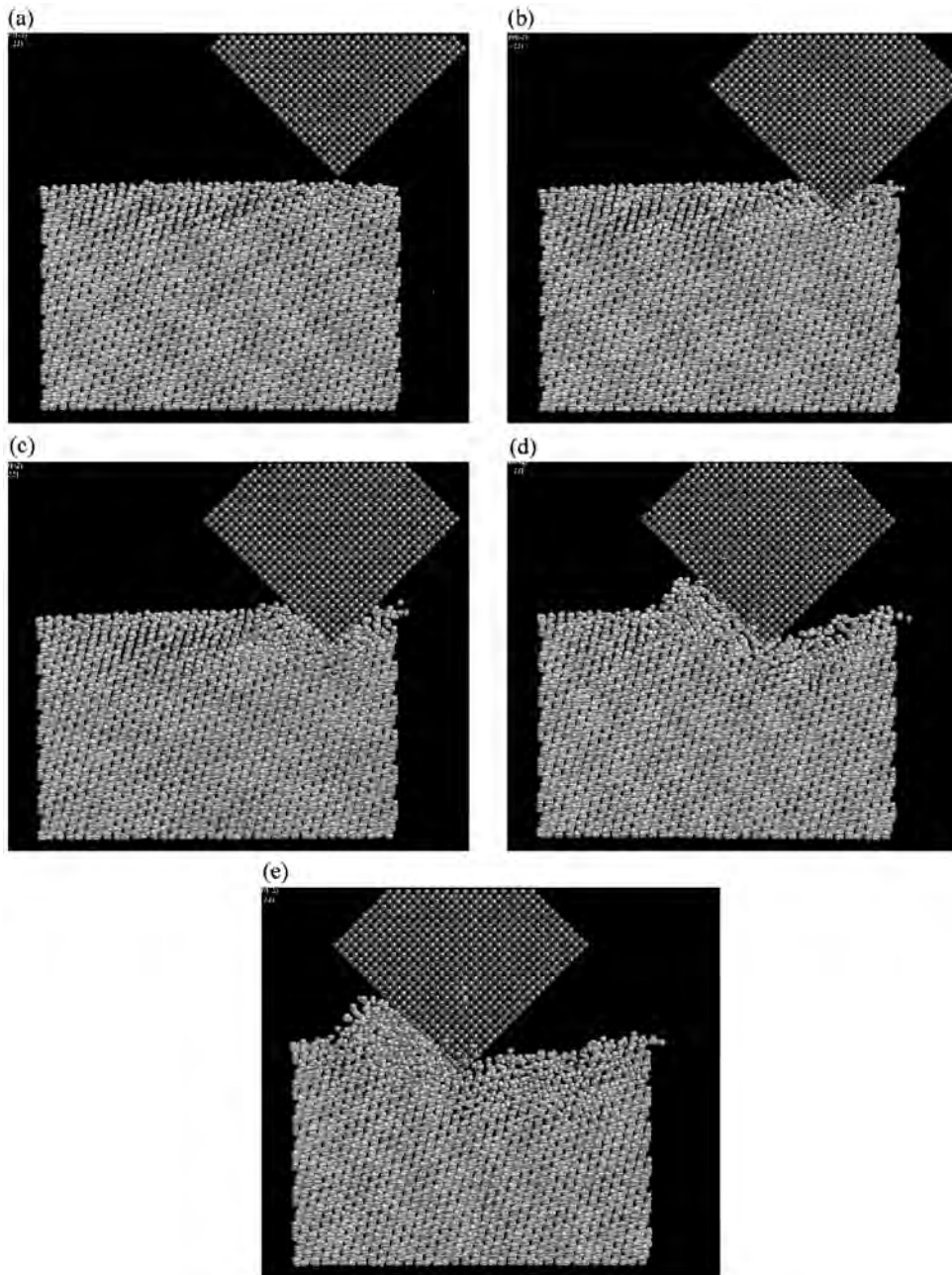
Figs. 17(a) to (h) shows the variation of the normal and tangential forces with distance along the direction of indentation prior to the contact of the indenter with the workmaterial for various crystal set-ups. It can be seen that as the indenter approaches the work, the force interactions commence at  $\sim 0.2$  nm. Coincidentally, this is about half the JC reported by Landman and Luedtke [39,40] and Buldum and Ciraci [60]. However, in their cases, both the workmaterial and the indenter are free to interact whereas in the present investigation, only the workmaterial is free and the indenter is infinitely rigid. Thus, the disturbance of the workpiece atoms when the indenter approaches nearly 0.2 nm appears reasonable. The workmaterial in the pre-



Figs. 15. (a)–(e) MD simulation plots showing various stages of the indentation–scratch test with the workmaterial set-up in the  $(\bar{1}20)[210]$  orientation.

sent investigation is aluminum whereas Landman and Luedtke were using gold and Buldum and Ciraci were using nickel as the work material, respectively. Consequently, the work material properties used are different and this can also account partially for the differences in the magnitude of the initial forces prior to the contact of the indenter. Also, the surfaces of the workmaterial in different orientations are not atomically smooth but are affected by the size of the atoms, the lattice spacing, the crystallographic orientation, and the direction of sliding. Thus, roughness of the surface on an atomic level will vary depending on the workmaterial as well as its crystallographic orientation and this can affect the initial forces as the indentation process commences.

The frequency of oscillation as well as the magnitudes of the forces tend to vary with the crystallographic orientations. It can be seen that maximum force variations occur in the case of  $(111)[\bar{1}10]$  and  $(111)[\bar{2}11]$  crystal set-ups. This is reflected by significant disturbance of the workmaterial in both the cases (Figs. 3(a) and 5(a)). It is, however, not clear why the magnitude of force is not significantly higher in the former case, as significant disturbance in the form of inverted trapezium is observed in the first case and less disturbance, only trigons in the second case. In the case of  $(001)[\bar{1}10]$ ,  $(110)[001]$ , and  $(001)[100]$  combinations, there is some disturbance of the workmaterial atoms near the surface and this is reflected by a smaller magnitude of the forces. In contrast, very little disturbance of the



Figs. 16. (a)–(e) MD simulation plots showing various stages of the indentation–scratch test with the workmaterial set-up in the  $(01\bar{2})[221]$  orientation.

workmaterial atoms was observed in the cases of  $(\bar{1}20)[210]$  and  $(110)[\bar{1}10]$ , and this is reflected by the very small variation of the forces not until the indenter is close to 0.05 nm from the workmaterial surface.

#### 4.3. Some quantitative analysis of the lattice disturbances, subsurface deformation, and chip volume

An attempt is made to quantitatively estimate the lattice disturbance prior to indentation, subsurface deformation at maximum indentation depth and after scratching, elastic

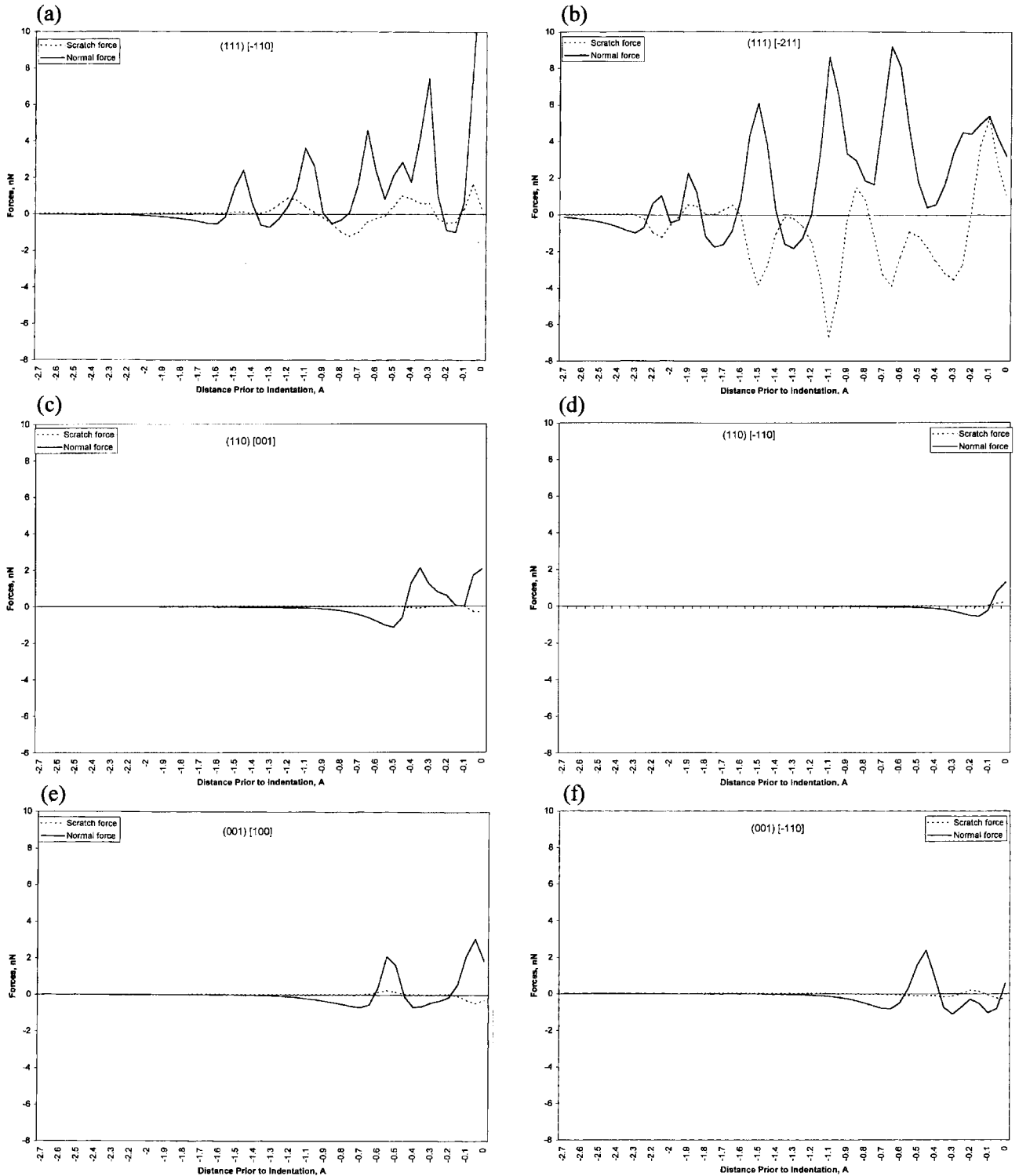
recovery, and number of atoms in the chip after scratching for various crystal orientations and scratch directions. For this, the workmaterial was divided into various zones (42 zones) as shown schematically in Fig. 18. In order to evaluate the above quantities, a parameter termed, “atom count ratio” is defined as follows:

$$\text{Atom count ratio } (R) = \frac{N_t}{N_{eq}},$$

where,  $N_t$  and  $N_{eq}$  are the number of atoms in a particular zone at time  $t$  and at equilibrium, respectively. This ratio

was evaluated at three time instants, namely, prior to indentation, at maximum indentation depth, and after retraction and plotted against the corresponding zone number. Standard deviation of the atom count ratio from the

mean was also evaluated for different combinations of crystal orientation. The biased method (*n*-method) was used for evaluating the standard deviation of the atom count ratio curves which specifies how widely the ratio is



Figs. 17. (a)–(h) Variation of normal and tangential forces with distance from the workmaterial as the indenter approaches the workmaterial in different crystallographic orientations.prior to tool contact with the workmaterial.

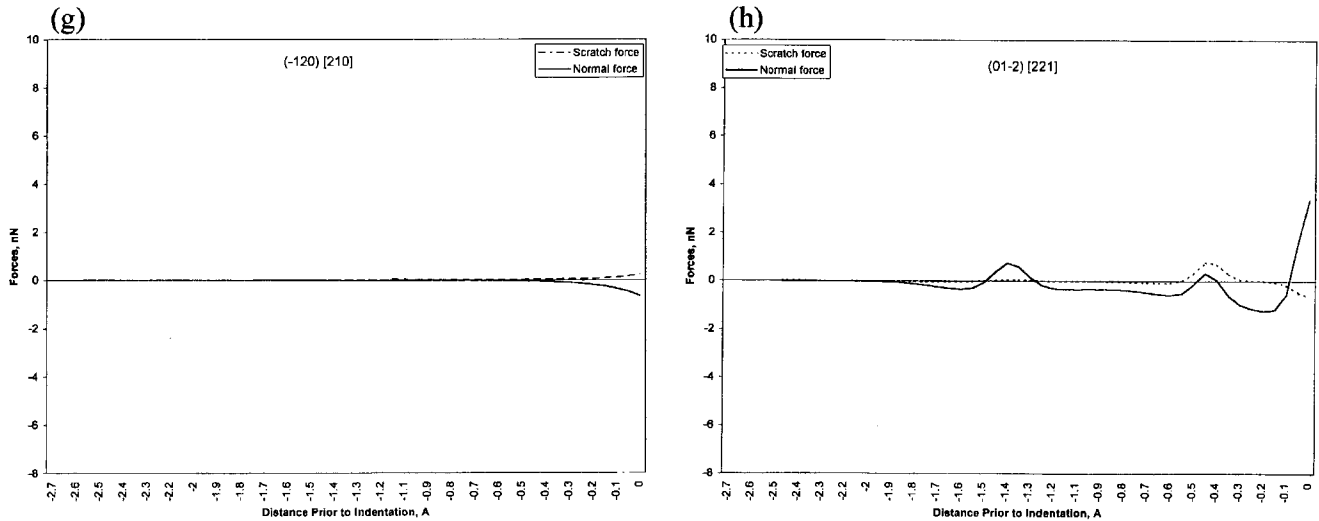


Fig. 17 (continued).

dispersed from the average value of 1. The formula used to determine the standard deviation of the atom count ratio is given in the following:

$$\sqrt{\frac{n\sum x^2 - (\sum x)^2}{n^2}}$$

where,  $x$  is the value of the atom count ratio and  $n$  is the total number of values which is 42 (the number of zones in the workmaterial).

Figs. 19(a)–(h) shows the variation of the atom count ratio in various zones for different combinations of crystal orientation and scratch direction, respectively. It can be seen from these figures that the atom count ratio of zones 1 through 24 are nearly unaffected by the indentation–scratching process. This suggests that the workmaterial size in the current study is sufficient to minimize or avoid boundary effects due to the indentation/scratching pro-

cess. With some combinations, for example,  $(111)\bar{2}11$  (Fig. 19(b)) we observe minor fluctuations of the atom count ratio in zones 1 through 24. This is attributed to the movement of a few atoms across the zone boundaries, which are strictly defined. When the coordinates of these atoms were monitored, it was observed that the change was in the 4th or 5th decimals. This small change can be due to the atomic vibrations or shock waves propagated through the crystal during scratching. This can result in a change in the atom count ratio. Consequently, these small variations are not considered as lattice disturbances but rather as the dynamic fluctuation of the atom count ratio. It is interesting to note that the dynamic fluctuation of the atom count ratio is different for different crystallographic orientations. If one would consider these fluctuations to be due to atomic vibrations or shock waves then it is appropriate to consider that these properties also vary with crystal orientation and scratch direction.

In the following, atom count ratio plots for two combinations, namely,  $(111)\bar{1}10$  (Fig. 19(a)) and  $(110)\bar{1}10$  (Fig. 19(c)) will be discussed in some detail for a better appreciation of the nature of their variation. Compare the atom count ratio plots prior to indentation in Fig. 19(a) and (c). Fig. 19(a) shows that the atom count ratio prior to indentation varies significantly and this extends till zone 26 while Fig. 19(c) shows lower variation, which extends only till zone 33. This suggests higher lattice disturbances in the case of  $(111)\bar{1}10$  combination compared to  $(110)\bar{1}10$  combination. This was also observed earlier from Figs. 3(a) and 9(a). At maximum indentation depth, the atom count ratio in zone 41 is significantly low for both combinations. This is because this zone is the indented zone and the atoms in this zone are being pushed to the side and lower zones. Consequently, both plots show an increase in the atom count ratio in zones 42, 40, 39, 36, 35, and 34 which are the zones immediately surrounding

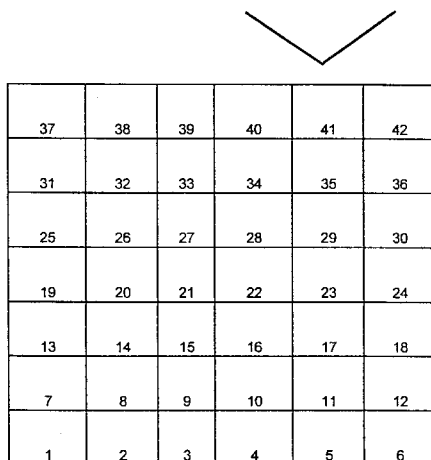
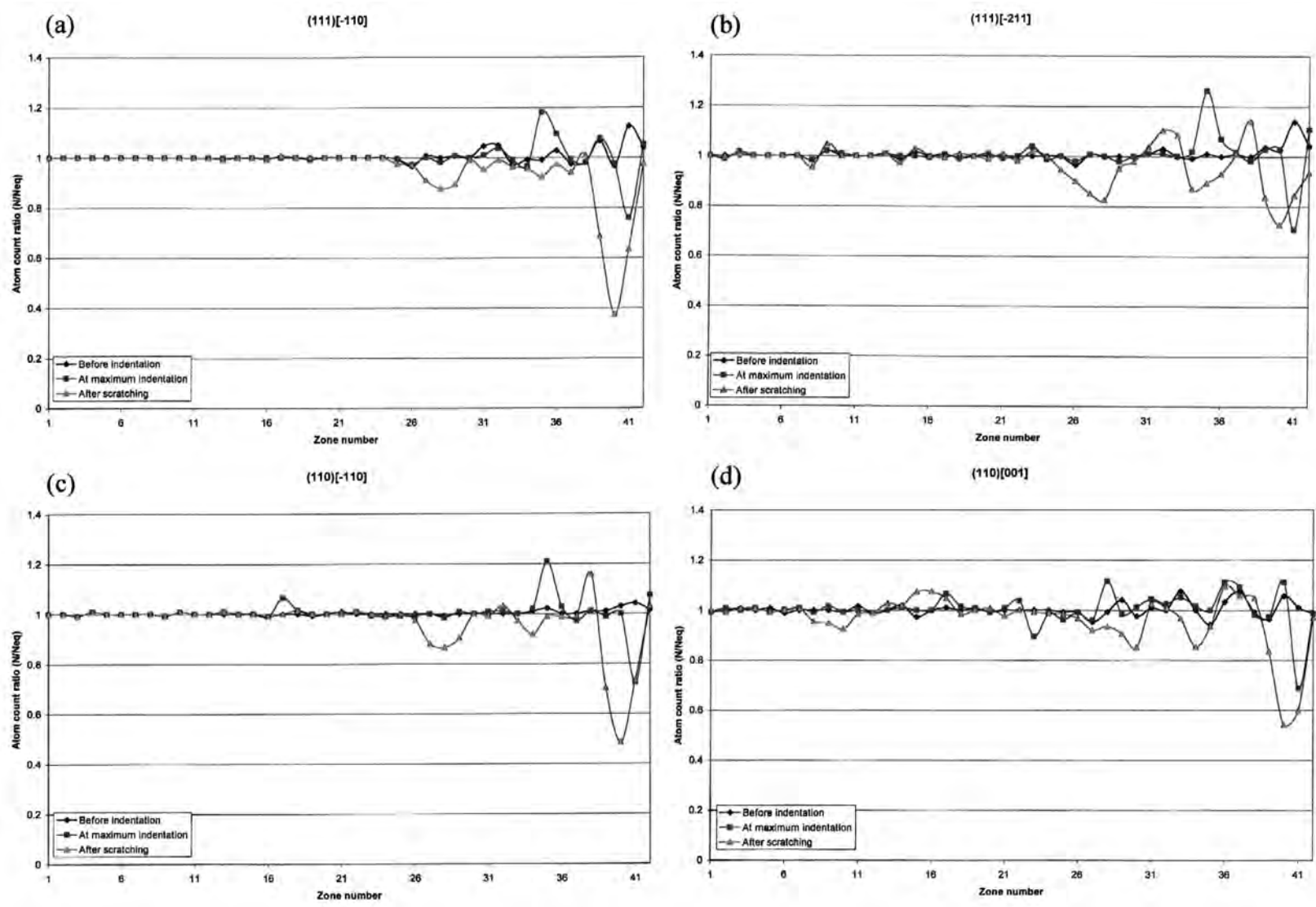


Fig. 18. Schematic of the workmaterial showing the division of workmaterial into various zones.



Figs. 19. (a)–(h) Variation of the atom count ratio in various zones for different combinations of crystal orientations and scratch directions.

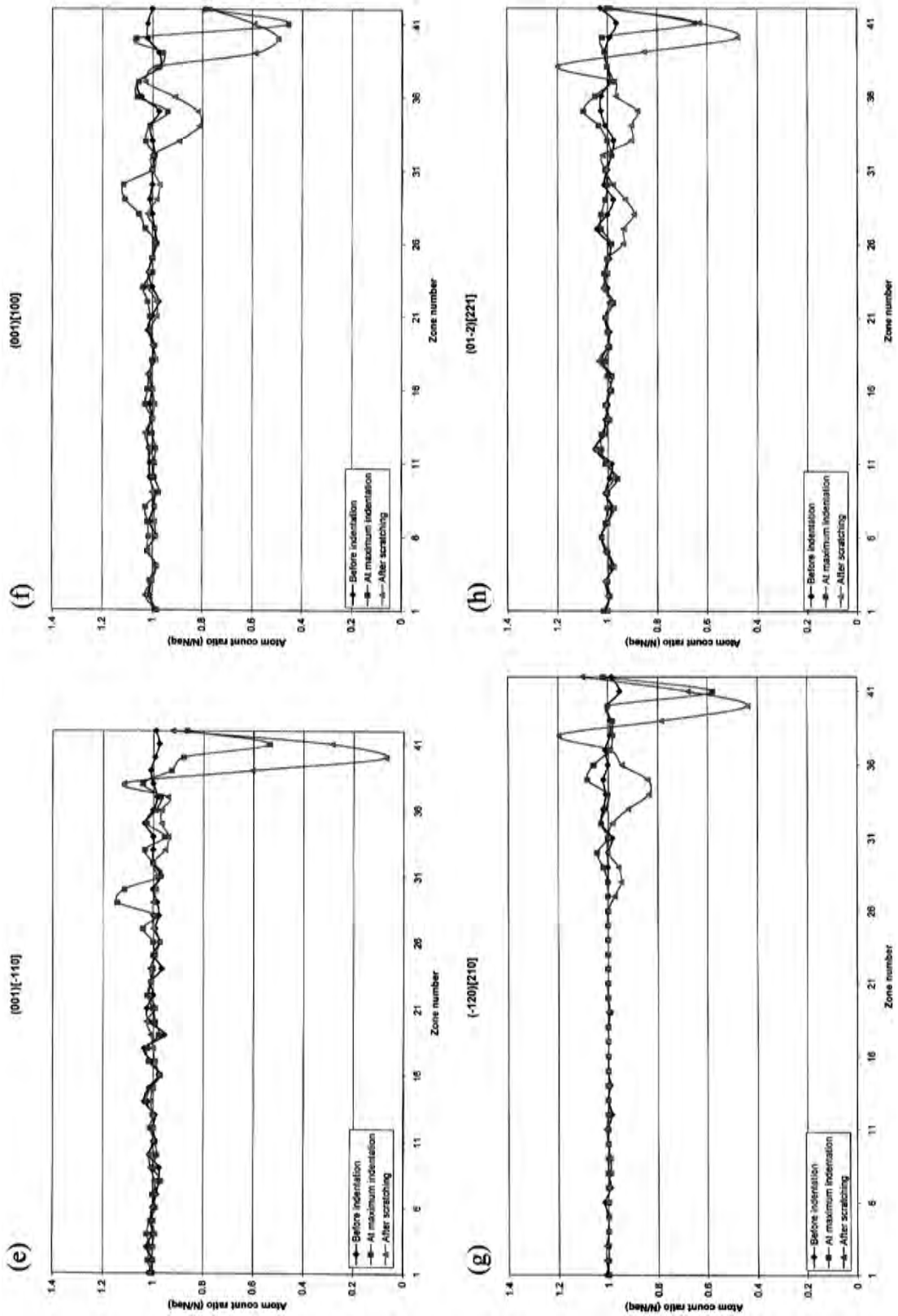


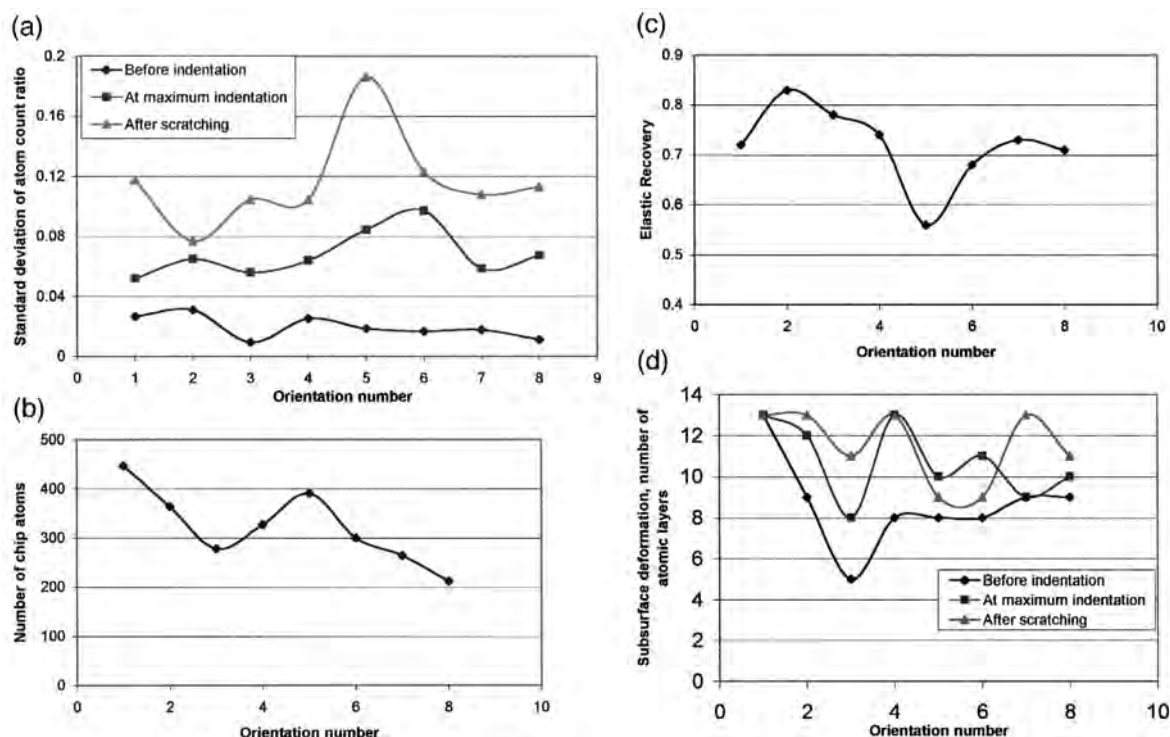
Fig. 19 (continued).

the indent. The increase in the atom count ratio for zone 35 is slightly higher in the case of  $(110)[\bar{1}10]$  combination (Fig. 19(c)) compared to  $(111)[\bar{1}10]$  combination (Fig. 19(a)). This can be attributed to the dislocations propagating parallel to the indentation direction with  $(110)[\bar{1}10]$  combination (Fig. 9(c)) which were not observed with the  $(111)[\bar{1}10]$  combination (Fig. 3(c)). In the case of  $(110)[\bar{1}10]$  (Fig. 19(c)), the atom count ratio remains around 1 from zone 26 to zone 18. However, zone 17 shows an increase in the atom count ratio. Once again, this can be due to the dislocations propagating parallel to the indentation direction with this particular combination. With  $(110)[\bar{1}10]$ , we observe the indentation damage to penetrate deep into the workmaterial (Fig. 19(c)), but the radius of the damaged zone (Fig. 9(c)) was not large in comparison to  $(111)[\bar{1}10]$  combination (Fig. 3(c)). Similar analysis was also applied to the atom count ratio after scratching and repeated for the other orientations as well.

Figs. 20(a)–(d) show the variation of standard deviation of atom count ratio, number of chip atoms, elastic recovery, and subsurface deformation for various orientations. Table 4 tabulates the corresponding numerical values. In this table, each combination of crystal orientation is given an orientation number which is used in Fig. 20(a–d). The elastic recovery was estimated as the ratio of the number of total atoms in zones 33, 34, 35, 39, 40, and 41 (Fig. 18) after scratching to that at equilibrium. Higher this ratio, higher is the elastic recovery of the orientation. Subsurface deformation prior to indentation, at maximum indentation

depth, and after scratching are estimated from the atom count ratio plots. Based on the deviation of the atom count ratio from its mean value, the zone till which damage extends is evaluated. From this, the subsurface deformation is defined in terms of the number of atomic layers. The subsurface deformation prior to indentation refers to the lattice disturbance as the indenter approaches the workmaterial surface. It should be noted that while the subsurface deformation for two orientations might be the same in terms of number of atomic layers along the depth direction, it might vary significantly in its radius. Hence, caution may have to be exercised at times when interpreting the results quantitatively.

Fig. 20(a) shows a high value of the standard deviation of atom count ratio prior to indentation for  $(111)[\bar{1}10]$  and  $(111)[\bar{2}11]$  combinations. This suggests high lattice disturbances prior to indentation for these two combinations. The lowest is observed with  $(110)[\bar{1}10]$  combination. Similar results were also observed from the MD simulation plots (Figs. 3(a), 5(a), and 9(a)). At maximum indentation depth, the standard deviation was found to be maximum with  $(001)[100]$  combination and minimum with  $(111)[\bar{1}10]$  combination. After scratching, the standard deviation was maximum with  $(001)[\bar{1}10]$  combination and minimum with  $(111)[\bar{2}11]$  combination. Fig. 20(b) shows the variation of the number of chip atoms showing a maximum with  $(111)[\bar{1}10]$  combination and minimum with  $(\bar{1}20)[210]$  combination. Fig. 20(c) plots the variation of elastic recovery with orientation where maximum and minimum elastic



Figs. 20. (a)–(d) Variation of (a) standard deviation of atom count ratio (b) number of chip atoms (c) elastic recovery and (d) subsurface deformation for various crystal orientations and scratch directions.

Table 4

Quantitative estimates of the standard deviation of atom count ratio, chip atom count, elastic recovery, and subsurface deformation for various combinations of crystal orientation and scratch direction

Crystal no.	Crystal orientation	Standard deviation of atom count ratio			Chip atom count	Elastic recovery	Subsurface deformation, number of atomic layers		
		Before indentation	At maximum indentation depth	After scratching			Before indentation	At maximum indentation depth	After scratching
1	(111)[−110]	0.0268	0.0519	0.1176	447	0.72	13	13	13
2	(111)[−211]	0.031	0.0649	0.0767	364	0.83	9	11	13
3	(110)[−110]	0.0094	0.0561	0.1044	278	0.78	5	8	11
4	(110)[001]	0.0253	0.064	0.1044	327	0.74	8	19	13
5	(001)[−110]	0.0185	0.0844	0.186	391	0.56	8	10	9
6	(001)[100]	0.0169	0.097	0.123	300	0.68	8	11	9
7	(01−2)[221]	0.0177	0.0587	0.108	264	0.74	9	9	13
8	(−120)[210]	0.0114	0.0673	0.113	212	0.71	9	10	11

recovery are observed with (111) $\bar{[2]11}$  and (001) $\bar{[1]10}$  combinations, respectively. This is in agreement with the MD simulation plots (Figs. 5(e) and 13(e)). Fig. 20(d) shows the variation of the subsurface deformation for various orientations prior to, at maximum depth, and after scratching. Prior to indentation, the maximum and minimum subsurface deformation were observed with (111) $\bar{[1]10}$  and (110) $\bar{[1]10}$  combinations, respectively which is in agreement with the simulations (Figs. 3(a) and 9(a)). A similar interpretation was made earlier based on the forces prior to indentation (Figs. 17(a–h)). A comparison of the MD simulation plots discussed earlier with the subsurface deformation curves at maximum indentation depth and after scratching (Fig. 20(d)) also show good agreement.

#### 4.4. On the nature of variation of forces and energy

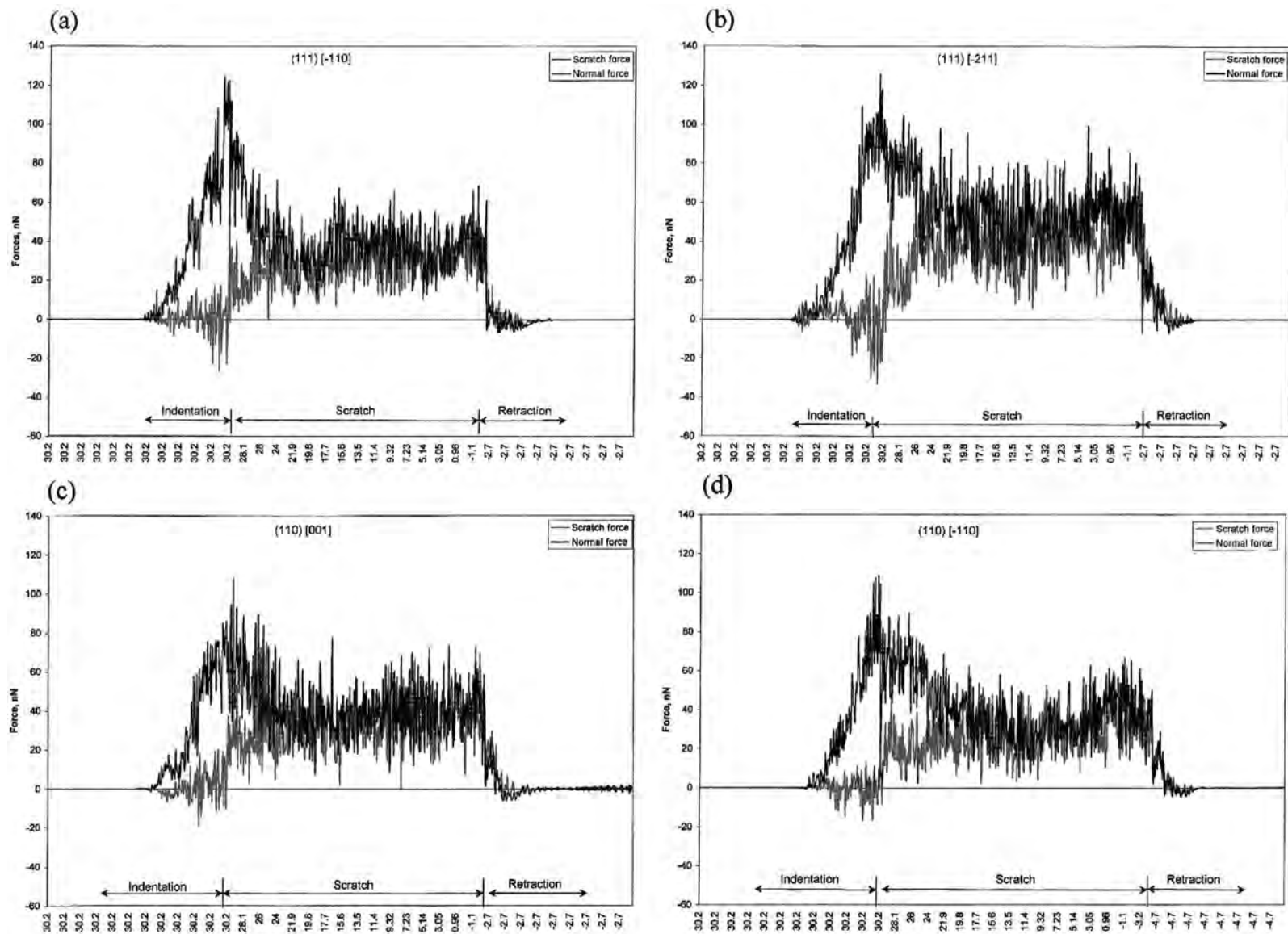
In general, indentation tests are conducted at constant load. However, in the present investigation, a constant velocity condition is used instead, for convenience. Consequently, the indentation force is taken as the average of the forces during the entire indentation process. The hardness of the workmaterial is evaluated as the average normal force over the contact area of the indenter with the workmaterial. The scratch force and the normal force are taken as the average of the corresponding steady state forces during the entire scratching process. The resultant force is taken as the vectorial sum of the scratching force and the normal force. They are subsequently normalized to force/unit width of scratch. The specific energy is defined as the energy required for removing unit volume of the workmaterial. The friction coefficient is evaluated as the ratio of the scratch force over the normal force, where the forces are the average values over the scratch length. The scratch hardness was calculated as the average scratch force during scratching over the deformation supporting area of the indenter.

Figs. 21(a) to (h) are the scratch and normal force–displacement curves obtained in MD simulation of indentation and scratching for different orientations and scratch

directions. The displacement axis gives the position of the tool-tip along the scratch direction. During indentation and retraction, the tool-tip position in the scratch direction (y-axis) remains constant and changes during scratching as indicated in Figs. 21(a) to (h). These plots provide the raw data for further analysis. Table 5 summarizes the results of the MD simulation studies of indentation–scratching conducted on a single crystal aluminum for different orientations and directions of scratching. It shows the magnitude of the scratching force, the normal force, the resultant force, the specific energy, friction coefficient, indentation hardness, and scratch hardness for various orientations and scratch directions.

In the following, the nature of the force–displacement curves will be discussed for a specific combination, i.e.  $\{001\}\langle 100 \rangle$  as an example. The repulsive force is considered positive. During indentation, the normal force increases rapidly and the tangential force remains almost zero. The increase in the forces though exhibits minor fluctuations is essentially uniform. After the indentation process, when the indenter was slid along the scratch direction, the normal force drops significantly. Further, during the scratch process, the primary force is along the scratch direction and hence the normal force drops significantly. However, it can be noted from the figure that the scratching force increases with a drop in the normal force. It can also be noted from the figure that the scratching force is lower than the normal force (also taken as the average values in Table 5) during sliding as the indenter presents a high negative rake angle ( $-45^\circ$ ) during the sliding process. Once the indenter has moved through the specified scratch distance, it was retracted from the workmaterial. The force corresponding to this segment of the simulation drops to zero as the tool-work separation increases. Hysteresis in the indentation–retraction curve can also be seen.

Fig. 22 shows the variation of hardness for different combinations of crystal setups. They were represented with increasing angle between the (111) and other planes considered here. It can be seen that the calculated hardness



Figs. 21. (a)–(h) Force–displacement curves obtained in MD simulation of indentation and scratching for different orientations and scratch directions.

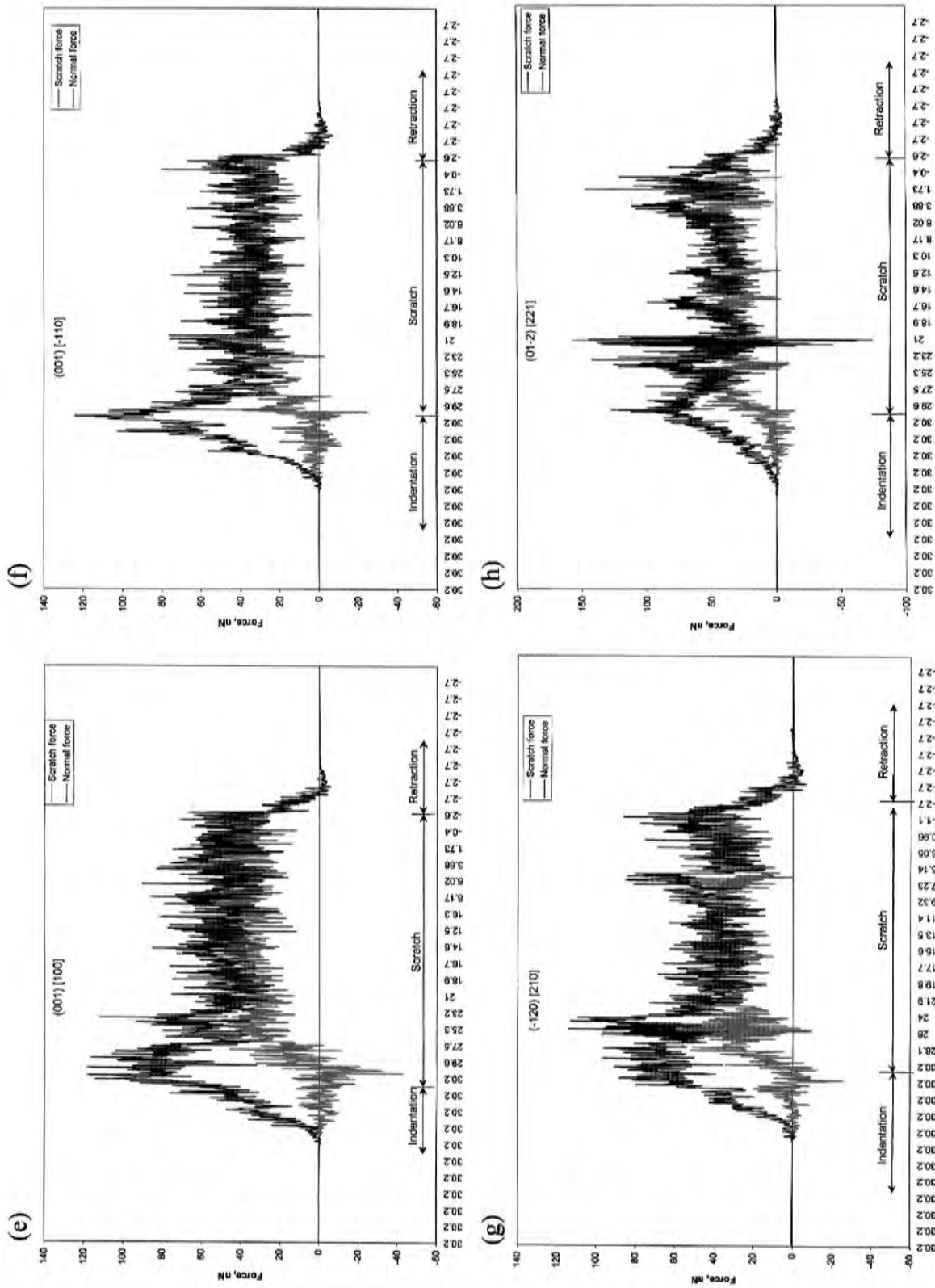


Fig. 21 (continued).

Table 5

Results of MD simulation of nanoindentation–scratch conducted on single crystal aluminum for different orientations

No.	Crystal orientation	Scratch force/unit width, ( $F_c$ ), N/mm $\times 10^2$	Normal force/unit width, ( $F_t$ ), N/mm $\times 10^2$	Friction coefficient ( $F_c/F_t$ )	Resultant force/unit width, ( $F_R$ ), N/mm $\times 10^2$	Specific energy, N/mm <sup>2</sup> $\times 10^{-5}$	Indentation hardness, GPa	Scratch hardness, GPa
1	(111) $\bar{1}$ 10	1.193	1.556	0.767	1.960	0.147	4.797	15.624
2	(111) $\bar{2}$ 11	1.590	2.278	0.698	2.778	0.196	4.933	22.879
3	(110) $\bar{1}$ 10	1.076	1.666	0.646	1.983	0.133	4.251	16.733
4	(110)[001]	1.319	1.709	0.772	2.159	0.163	3.982	17.165
5	(001) $\bar{1}$ 10	1.297	1.567	0.828	2.034	0.160	5.063	15.738
6	(001)[100]	1.485	2.127	0.698	2.594	0.183	5.068	21.360
7	( $\bar{1}$ 20)[210]	1.299	1.894	0.686	2.297	0.1604	3.891	19.023
8	(01 $\bar{2}$ )[221]	1.551	2.108	0.736	2.617	0.191	3.599	21.172

values are an order of magnitude higher than the engineering values. This can be attributed to the fact that the depth of indentation is significantly smaller and at such small scales of indentation, it is possible that plastic deformation is governed by the theoretical yield strength. This increase is attributed to the well-known Size effect. Belak et al. [35] reported in the MD simulation of indentation of silver substrate, a hardness of 5.4 GPa which is close to the theoretical hardness value of 4.5 GPa. They also proposed a similar rationale for the high values. It can also be noted from Fig. 22 that the hardness value is not only a function of the indentation direction or plane of indentation alone but also depends on the crystal orientation. In Table 5,  $z$  represents the plane of indentation as well as the direction of indentation since indentation was performed perpendicular to the  $z$  plane. It can be noted that the calculated hardness value show variation even when the plane of indentation and the indentation direction maintained constant. Among the orientations studied, the maximum hardness value is found with the (001)[100] combination and the minimum hardness direction [100] is in fact the same as the

indentation direction of maximum hardness proposed by Garfinkle and Garlick [18]. For the combinations studied, Fig. 22 also shows the anisotropy to be the least for the (001) orientation with indentation performed along [001] direction. The hardness variation is found to be maximum for the (110) orientation with the indentation performed along the [110] direction (Fig. 22). From Table 5, the

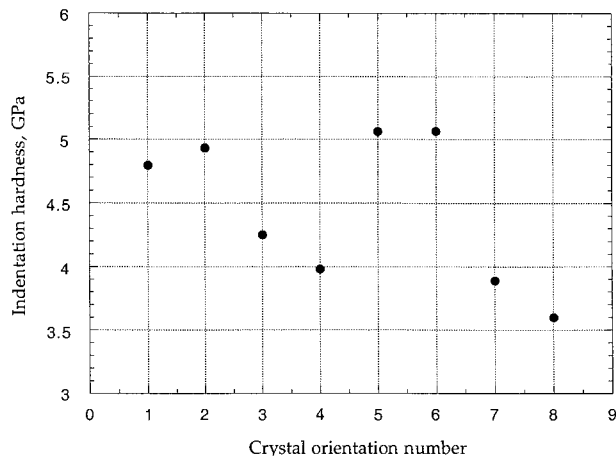
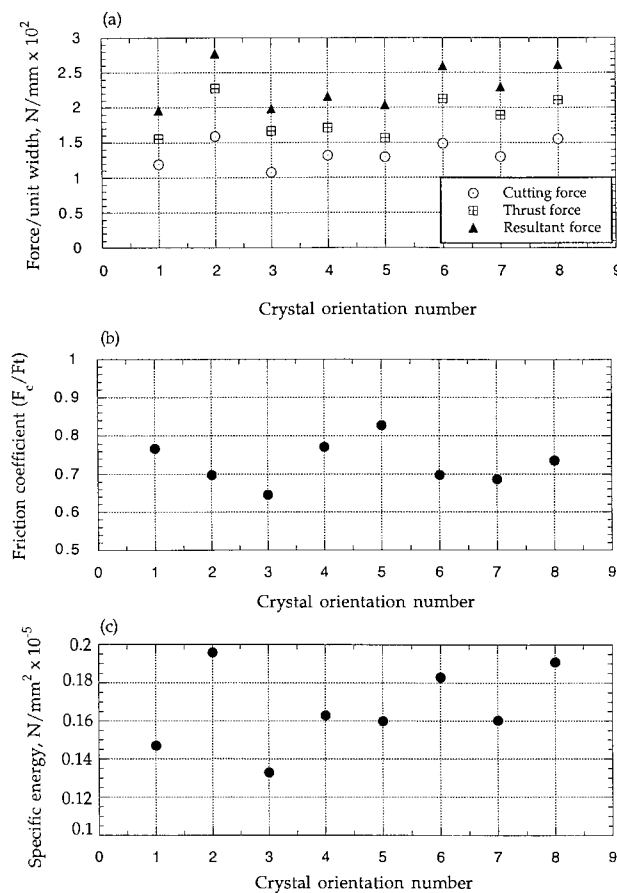


Fig. 22. Variation of hardness for different combinations of orientations and scratch directions.



Figs. 23. (a)–(c) Variation of the cutting force, the thrust force, the resultant force, (b) the friction coefficient, and (c) the specific energy during the scratch process for various combinations of crystal orientations and scratch directions.

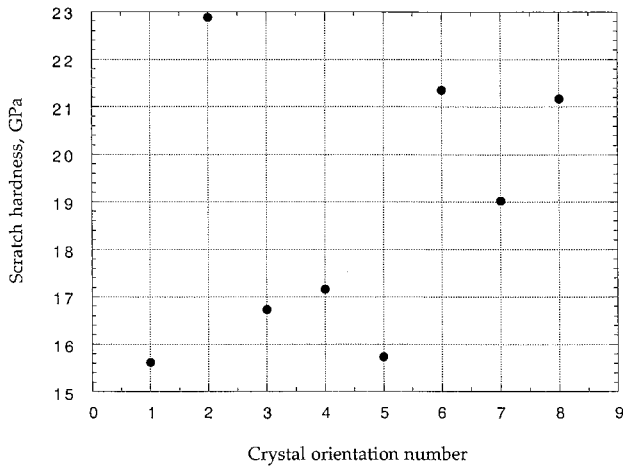


Fig. 24. Variation of scratch hardness for different combinations of orientations and scratch directions.

hardness anisotropy of aluminum with different crystal set-up is calculated to be  $\sim 29\%$  which is close to the anisotropy of this material in the elastic range (21.9%). A similar anisotropy is anticipated in the plastic range.

Figs. 23(a)–(c) show the variation of the scratching force, the normal force, the resultant force, the friction coefficient, and the specific energy during the scratch process for various combinations of crystal set-ups. Fig. 23(a) is the variation of the scratching force, the normal force, and the resultant force with crystal orientation. Minimum in the scratching force was obtained along the  $(110)[\bar{1}10]$  orientation and maximum along the  $(111)[\bar{2}11]$  orientation. This is not in total agreement with the argument that the minimum scratching force for an FCC

material should be along the most favorable slip system, i.e. in the  $(111)[\bar{1}10]$  combination. However, the indenter used here had a high negative rake of  $-45^\circ$  and consequently, the normal force during scratching would be the dominant force. It, therefore, appears that the theoretical predictions regarding the magnitude of forces with orientation should perhaps be considered for the normal force and not for the scratching force. It can be seen that from Fig. 23(a), the minimum normal force is along the  $(111)[\bar{1}10]$  orientation, which is the most favored slip system for an FCC material. This reasoning is substantiated by similar trends in the resultant force and the normal force (Fig. 23(a)), which show minimum and maximum values along  $(111)[\bar{1}10]$  and  $(111)[\bar{2}11]$ , respectively. In an earlier MD simulation study on the effect of crystal orientation and cutting direction of aluminum single crystals [2] with a positive rake tools, the minimum and the maximum forces were experienced with the  $(111)[\bar{1}10]$  combination and the  $(110)[001]$  combination, respectively. The differences in the results once again highlights the influence of the tool geometry on the resultant force system.

Fig. 23(b) shows the variation of friction coefficient with crystal orientation. Friction coefficient is calculated as the ratio of the scratching force to the normal force. The highest friction coefficient is found to be along the  $(001)[\bar{1}10]$  orientation and the lowest along the  $(110)[\bar{1}10]$  orientation. The friction coefficients obtained in this investigation are high and in the range of 0.6–0.9. Eventhough the loads are significantly low, the friction coefficients are higher. The high friction coefficients observed in this study are attributed to the material removal in scratching with a high negative rake tool ( $-45^\circ$ ). In general, the friction

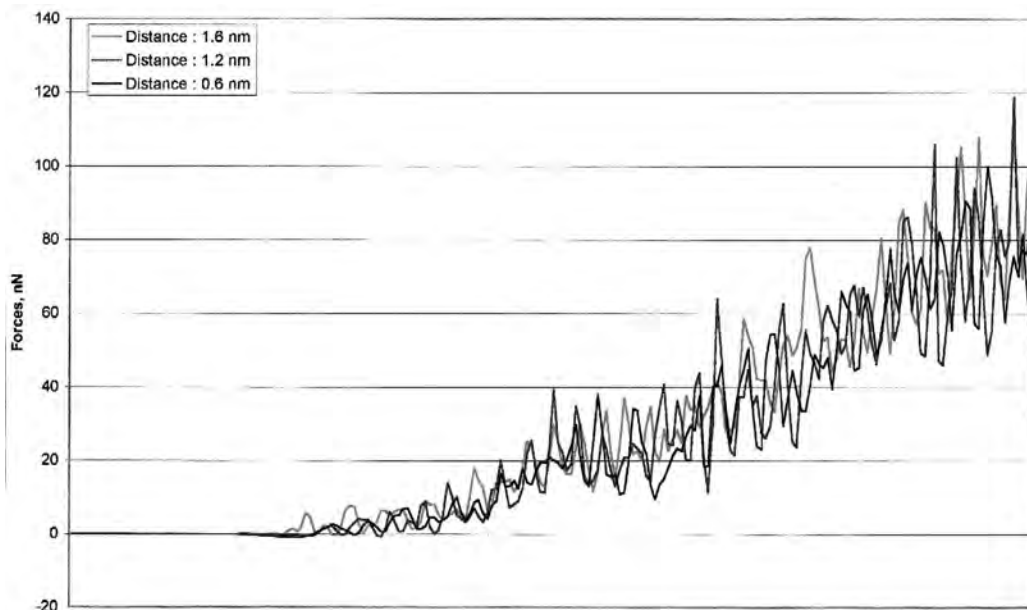


Fig. 25. Indentation curves for simulations on  $(110)[\bar{1}10]$  combination started at various time instants in order to estimate the statistical error of indentation hardness.

coefficient in grinding where the abrasives present a high negative rake angle ( $\sim -60^\circ$ ) is estimated to be  $\sim 0.5$  [67]. In the present investigation, the indenter presents a high negative rake angle of  $-45^\circ$  during the scratch process. The large negative rake angles, in general, are typical for most indenter geometries. Consequently, even though the normal force (load) is significantly low (nN range) the tool nomenclature results in an approximately equivalent decrease in the scratch force. This can result in high friction coefficient even with loads in the nN range. It is also possible that the contact pressure exerted by the tool can be significantly higher resulting in increased friction coefficient values.

The friction coefficient shows maximum variation with scratch direction when sliding along the (110) plane (16.32%). This is followed by (001) (15.7%) and the minimum (9%) with (111) plane. This is attributed to the fact that the (110) is the least packed plane and (111) is the most packed plane with (001) in between.

Fig. 23(c) shows the variation of specific energy with crystal orientation. It follows a similar trend as the cutting force (Fig. 23(a)). Fig. 24 shows the variation of the scratch hardness with crystal orientation. It was found to be minimum along the (111) $\bar{1}10$  orientation and maximum along the (111) $\bar{2}11$  orientation (Fig. 24 and Table 5). The anisotropy of scratch hardness of single crystal aluminum was found to be in the range of 30%.

In order to estimate the statistical error of the numerical quantities evaluated, for example, indentation hardness, three indentation simulations were performed (for a particular crystal orientation, namely, (110) $\bar{1}10$ ) with the indentation process starting at various time instants. This was achieved by altering the initial position of the tool relative to the surface of the workmaterial. This process will have some effect on the atom positions as the equations of motion are being evaluated for various time intervals before indentation begins. Fig. 25 plots the indentation curves for the three simulations mentioned above. It can be observed from this figure that apart from small variations in the dynamic fluctuations, the variations in the force curves are insignificant. Table 6 tabulates the indentation hardness for simulations starting at various time instants. It can be observed that the error between the indentation hardness values is less than 2%.

Table 6  
Statistical error estimate of indentation hardness for (110) $\bar{1}10$  orientation

No.	Distance of indenter from workmaterial surface, nm	Time before indentation begins, $s \times 10^{-14}$	Indentation hardness, GPa	Error, %
1	1.6	320	4.25	0
2	1.2	240	4.20	1.2
3	0.6	120	4.18	1.7

## 5. Conclusions

Molecular Dynamics (MD) simulation of indentation–scratching was conducted on single crystal aluminum in different orientations and scratch directions, namely,  $\{(111)\bar{1}10, (111)\bar{2}11, (110)\bar{1}10, (110)001, (001)\bar{1}10, (001)100, \bar{1}20210, (01\bar{2})221\}$ , to investigate the extent of anisotropy in hardness and friction coefficient of this material. Specific conclusions that may be drawn from this study are given in the following. In some cases, only experimental observations are summarized as specific reasons for their behavior are not known at this stage.

(1) The calculated hardness values were found to be an order of magnitude higher than the engineering hardness values at the macrolevel and in the range anticipated at the nanolevel due to size effect. The magnitude of hardness was found to increase significantly as the indentation depths were reduced to atomic level.

(2) At very low indentation depths, i.e. nanoindentation, plastic deformation appears to be governed by the theoretical yield strength of the workmaterial, again due to the size effect.

(3) The hardness anisotropy of aluminum with different crystal set-ups was observed to be in the range of 29%. This may be compared to the anisotropy of this material in the elastic range (21.9%). It would be more useful to compare the anisotropy of this material in the plastic range, if available.

(4) Maximum hardness value was experienced with the (001)100 and the minimum with the (01 $\bar{2}$ )221. Anisotropy of hardness was observed to depend on the crystal orientation in addition to the indentation direction and the plane of indentation.

(5) During indentation, dislocations were observed to propagate both parallel and perpendicular to the indentation direction in the case of (110) $\bar{1}10$  orientation. In contrast, the dislocations were observed to propagate only parallel to the indentation direction in the case of (001) $\bar{1}10$  orientation. At other orientations, they were generally oriented at an angle to the direction of scratching which depends on the crystal orientation and the direction of scratching.

(6) Initial disturbance of the atoms near the surface of the workmaterial prior to indentation (i.e. as the indenter was brought close to the workmaterial), was observed to vary with crystallographic factors. This was observed to be maximum in the case of (111) $\bar{1}10$  followed by (111) $\bar{2}11$  orientation. Minimum disturbance of the top layers of the workmaterial was found to be in the case of (110)001 and (001) $\bar{1}10$  orientations. Insignificant or practically zero disturbance was observed for the remaining combinations investigated, namely, (110) $\bar{1}10$ , (001)100,  $\bar{1}20210$ , and (01 $\bar{2}$ )221. Instantaneous forces as the indenter approached the workmaterial in different crystallographic directions were found to correlate reasonably well with the degree of disturbance of the workmaterial.

(7) Friction coefficient, defined as the ratio of the scratching force to the normal force, during scratching was observed to be high, i.e. in the range of 0.6–0.9. Even though both the forces are very low, the friction coefficients are found to be rather high. This is attributed to the high negative rake angle ( $-45^\circ$ ) presented by the indenter and the resulting high contact pressure exerted by the indenter. During scratching, bonds between the atoms have to be broken and reformed at an atomic level and it may not be possible to have low friction coefficients unless the contact between them involves a physisorbed layer, as in van der Waals bonding.

(8) The resultant force during the scratch process was found to be minimum along the  $(111)\bar{1}10$  orientation and maximum along the  $(111)\bar{2}11$  orientation. The highest friction coefficient was observed to be along  $(001)\bar{1}10$  and the lowest along  $(110)\bar{1}10$  orientation. The reasons for this are not clear at this stage.

(9) The scratch hardness was observed to be minimum along the  $(111)\bar{1}10$  orientation and maximum along the  $(111)\bar{2}11$  orientation. The reasons for this, again, are not clear at this stage. The anisotropy of scratch hardness of aluminum was also found to be in the range of 30%.

(10) The extent of elastic recovery, subsurface deformation, and chip volume were found to vary with the crystallographic orientation.

## Acknowledgements

This project is sponsored by grants from the Manufacturing Processes and Machines Program (DMI-9523551) of the Division of the Design, Manufacture, and Industrial Innovation (DMII) and the Tribology and Surface Engineering Program (CMS 9414610) of the Division of Civil and Mechanical Structures of the National Science Foundation. The authors thank Drs. K.P. Rajurkar, Delcie Durham, B.M. Kramer, L. Martin-Vega of DMII and J. Larsen Basse of the Tribology and Surface Engineering Program for their interest in and support of this work. One of the authors (R.K.) also thanks the MOST Chair (Most Eminent Scholars Program) for enabling the preparation of the manuscript. The authors also thank Mr. Robert Stewart and Mr. P.R. Mukund for their contributions towards the development of the software for animation and initial indentation–scratching simulations. The authors thank the reviewers for their constructive criticism, valuable comments, and useful suggestions that enhanced the quality of the paper.

## References

- [1] R.W. Hertzberg, in: *Deformation and Fracture Mechanics of Engineering Materials*, 4th edn., Wiley, 1996, p. 14.
- [2] R. Komanduri, N. Chandrasekaran, L.M. Raff, M.D. simulation of nanometric cutting of single crystal aluminum-effect of crystal orientation and direction of cutting, *Wear* (2000).
- [3] H. Heinzelmann, E. Meyer, H. Rudin, H.J. Guntherodt, in: *Force Microscopy, Scanning Tunneling Microscopy and Related Methods*, 1990, p. 443.
- [4] S.R. Cohen, G. Neubauer, G.M. McClelland, Nanomechanics of Au–Ir contact using a bidirectional atomic force microscope, *J. Vac. Sci. Technol. A* 8 (1990) 3449.
- [5] M. Hirano, K. Shinjo, Superlubricity and frictional anisotropy, *Wear* 168 (1993) 121.
- [6] J.J. Vlassak, W.D. Nix, Measuring the elastic properties of anisotropic materials by means of indentation experiments, *J. Mech. Phys. Solids* 42 (8) (1994) 1223.
- [7] M.F. Doerner, W.D. Nix, A method for interpreting the data from depth sensing indentation instruments, *Mater. Res.* 1 (1986) 601.
- [8] R. Komanduri, D.A. Lucca, Y. Tani, Technological advances in fine abrasive processes, *Ann. CIRP* 46 (2) (1997) 545.
- [9] R. Komanduri, N. Chandrasekaran, L.M. Raff, Effect of tool geometry in nanometric cutting: a molecular dynamics simulation approach, *Wear* 219 (1998) 84.
- [10] G.E. Dieter, in: *Mechanical Metallurgy*, 3rd edn., McGraw-Hill, New York, NY, 1986.
- [11] F.P. Bowden, C.A. Brookes, Frictional anisotropy in non-metallic crystals, *Proc. R. Soc. London A* 295 (1966) 244.
- [12] C.A. Brookes, J.B. O'Neill, B.A.W. Redfern, Anisotropy in the hardness of single crystals, *Proc. R. Soc. London A* 322 (1971) 73.
- [13] N. Gane, F.P. Bowden, Microdeformation of solids, *J. Appl. Phys.* 39 (1968) 1432–1435.
- [14] C.C. Chen, A.A. Hendrickson, Dislocation etch pits in silver, *J. Appl. Phys.* 42 (1971) 2208.
- [15] G.M. Pharr, W.C. Oliver, Nanoindentation of silver-relations between hardness and dislocation structure, *J. Mater. Res.* 4 (1989) 94.
- [16] F.W. Daniels, C.G. Dunn, The effect of orientation on knoop hardness of single crystals of zinc and silicon ferrite, *Trans. Am. Soc. Met.* 41 (1949) 419.
- [17] E.R. Petty, The hardness anisotropy of aluminum single crystals, *J. Inst. Met.* 91 (1962) 54–62.
- [18] M. Garfinkle, R.G. Garlick, A stereographic representation of knoop hardness anisotropy, *Trans. Metall. Soc. AIME* 242 (1968) 809–814.
- [19] Y. Enomoto, D. Tabor, The frictional anisotropy of diamond, *Proc. R. Soc. London A* 373 (1981) 405.
- [20] R. Kaneko, K. Nonaka, K. Yasuda, Summary abstract: scanning tunneling microscopy and atomic force microscopy for microtribology, *J. Vac. Sci. Technol. A* 6 (1988) 291.
- [21] G.J. Germann, S.R. Cohen, G. Neubauer, G.M. McClelland, H. Seki, Atomic scale friction of a diamond tip on diamond (100) and (111) surfaces, *J. Appl. Phys.* 73 (1) (1993) 163.
- [22] N.P. Suh, N. Saka, Surface engineering, *Ann. CIRP* 36 (1987) 403.
- [23] D.E. Kim, N.P. Suh, On microscopic mechanisms of friction and wear, *Wear* 149 (1991) 199.
- [24] R. Erlandsson, G. Hadziioannou, C.M. Mate, G.M. McClelland, S. Chiang, Atomic scale friction between the muscovite mica cleavage plane and a tungsten tip, *J. Chem. Phys.* 89 (8) (1988) 5190.
- [25] C.M. Mate, G.M. McClelland, R. Erlandsson, S. Chiang, Atomic scale friction of a tungsten tip on a graphite surface, *Phys. Rev. Lett.* 59 (1987) 1942.
- [26] E. Rabinowicz, Friction coefficients of noble metals over a range of loads, *Wear* 159 (1992) 89.
- [27] B. Alder, T. Wainwright, Studies in molecular dynamics I. General method, *J. Chem. Phys.* 31 (1959) 459.
- [28] B. Alder, T. Wainwright, Studies in molecular dynamics: II. Behavior of a small number of elastic spheres, *J. Chem. Phys.* 33 (1960) 1439.
- [29] W.G. Hoover, in: *Molecular Dynamics, Lecture Notes in Physics*, Springer-Verlag, Berlin, 1986, p. 258.
- [30] W.G. Hoover, C.G. Hoover, I.F. Stowers, Interface tribology by

- nonequilibrium molecular dynamics, fabrication technology, Mater. Res. Soc. Symp. Proc. 140 (1989) 119.
- [31] W.G. Hoover, A.J. De Groot, C.G. Hoover, I.F. Stowers, T. Kawai, B.L. Holian, T. Boku, S. Ihara, J. Belak, Large scale elastic–plastic indentation simulations via non-equilibrium molecular dynamics, Phys. Rev. A 42 (10) (1990) 5844.
- [32] J. Belak, I.F. Stowers, A molecular dynamics model of the orthogonal cutting process, in: Proc. ASPE Annual Conf., Rochester, NY, 1990, p. 76.
- [33] J. Belak, D.A. Lucca, R. Komanduri, R.L. Rhorer, T. Moriwaki, K. Okuda, N. Ikawa, S. Shimada, H. Tanaka, T.A. Dow, J.D. Drescher, I.F. Stowers, Molecular dynamics simulation of the chip forming process in single crystal copper and comparison with experimental data, in: Proc. of the ASPE Annual Conference, 1991, p. 100.
- [34] J. Belak, in: Nanotribology: Modelling Atoms When Surfaces Collide, Energy and Technology Review, Lawrence Livermore Laboratory, 1994, p. 13.
- [35] J. Belak, D.B. Boercker, I.F. Stowers, Simulation of nanometer scale deformation of metallic and ceramic surfaces, MRS Bull. 18 (1993) 55.
- [36] U. Landman, W.D. Luedtke, M.W. Ribarsky, Micromechanics and microdynamics via atomistic simulations, Mater. Res. Soc. Symp. Proc. 140 (1989) 101.
- [37] U. Landman, W.D. Luedtke, N.A. Burnham, R.J. Colton, Atomistic mechanisms and dynamics of adhesion, nanoindentation, and fracture, Science 248 (1990) 454.
- [38] U. Landman, W.D. Luedtke, Nanomechanics and dynamics of tip-substrate interactions, J. Vac. Sci. Technol. 9 (1991) 414.
- [39] U. Landman, W.D. Luedtke, E.M. Ringer, Atomistic mechanisms of adhesive contact formation and interfacial processes, Wear 153 (1992) 3.
- [40] U. Landman, W.D. Luedtke, Atomistic dynamics of interfacial processes: films, junctions, and nanostructures, Appl. Surf. Sci. 92 (1996) 237.
- [41] N. Ikawa, S. Shimada, H. Tanaka, G. Ohmori, An atomistic analysis of nanometric chip removal as affected by tool-work interaction in diamond turning, Ann. CIRP 40 (1) (1991) 551.
- [42] S. Shimada, N. Ikawa, G. Ohmori, H. Tanaka, Molecular dynamics analysis as compared with experimental results of micromachining, Ann. CIRP 41 (1) (1992) 117.
- [43] S. Shimada, N. Ikawa, H. Tanaka, G. Ohmori, J. Uchikoshi, H. Yoshinaga, Feasibility study on ultimate accuracy in microcutting using molecular dynamics simulation, Ann. CIRP 42 (1) (1993) 91.
- [44] S. Shimada, N. Ikawa, H. Tanaka, J. Uchikoshi, Structure of micro-machined surface simulated by molecular dynamics analysis, Ann. CIRP 43 (1) (1994) 51.
- [45] S. Shimada, Molecular dynamics analysis of nanometric cutting process, Int. J. Jpn. Soc. Precis. Eng. 29 (4) (1995) 283.
- [46] T. Inamura, H. Suzuki, N. Takezawa, Cutting experiments in a computer using atomic models of copper crystal and a diamond tool, Int. J. Jpn. Soc. Precis. Eng. 25 (4) (1991) 259.
- [47] T. Inamura, N. Takezawa, N. Taniguchi, Atomic-scale cutting in a computer using crystal models of copper and diamond, Ann. CIRP 41 (1) (1992) 121.
- [48] T. Inamura, N. Takezawa, Y. Kumaki, Mechanics and energy dissipation in nanoscale cutting, Ann. CIRP 42 (1) (1993) 79.
- [49] T. Inamura, N. Takezawa, Y. Kumaki, T. Sata, On a possible mechanism of shear deformation in nanoscale cutting, Ann. CIRP 43 (1) (1994) 47.
- [50] K. Maekawa, A. Itoh, Friction and tool wear in nanoscale machining–molecular dynamics approach, Wear 188 (1995) 115.
- [51] N. Chandrasekaran, A. Noori-Khajavi, L.M. Raff, R. Komanduri, A new method for molecular dynamics simulation of nanometric cutting, Philos. Mag. B 77 (1) (1998) 7.
- [52] R. Komanduri, N. Chandrasekaran, L.M. Raff, Some aspects of machining with negative rake tools simulating grinding: an MD simulation approach, Philos. Mag. B 79 (7) (1999) 955.
- [53] O. Tomagnini, F. Ercolessi, E. Tosatti, Microscopic interaction between a gold tip and lead surface, Surf. Sci. 287/288 (1993) 1041.
- [54] D.W. Brenner, S.B. Sinnott, J.A. Harrison, O.A. Shenderova, Simulated engineering of nanostructures, Nanotechnology 7 (1996) 161.
- [55] R. Rentsch, I. Inasaki, Molecular dynamics simulation for abrasive processes, Ann. CIRP 43 (1) (1994) 327.
- [56] R. Rentsch, I. Inasaki, Indentation simulation on Brittle materials by molecular dynamics, SPIE 2596 (1995) 214.
- [57] J.A. Harrison, D.W. Brenner, C.T. White, R.J. Colton, Atomistic mechanisms of adhesion and compression of diamond surfaces, Thin Solid Films 206 (1991) 213.
- [58] W. Yan, K. Komvopoulos, Three dimensional molecular dynamics analysis of atomic scale indentation, J. Tribol. 120 (1998) 385.
- [59] J.A. Harrison, C.T. White, R.J. Colton, D.W. Brenner, Molecular dynamics simulations of atomic scale friction of diamond surfaces, Phys. Rev. B 46 (15) (1992) 9700.
- [60] A. Buldum, S. Ciraci, Contact, nanoindentation, and sliding friction, Phys. Rev. B 57 (4) (1998) 2468.
- [61] D.E. Kim, N.P. Suh, Molecular dynamics investigation of two dimensional atomic scale friction, ASME J. Tribol. 116 (1994) 225.
- [62] M. Hirano, K. Shinjo, Atomistic locking and friction, Phys. Rev. B 41 (17) (1990) 11837.
- [63] R. Komanduri, N. Chandrasekaran, MD simulation of atomic scale friction, Phys. Rev. (2000) in press.
- [64] N.A. Burnham, R.J. Colton, H.M. Pollock, Interpretation issues in force microscopy, J. Vac. Sci. Technol. A 9 (1991) 2548.
- [65] M. Salmeron, A. Folch, G. Neubauer, M. Tomitori, D.F. Ogletree, W. Kolbe, Nanometer scale mechanical properties of Au(111) thin films, Langmuir 8 (1992) 2832.
- [66] E.R. Marshall, M.C. Shaw, Forces in dry surface grinding, Trans. ASME 74 (1952) 51.
- [67] R. Komanduri, Some aspects of machining with negative rake tools simulating grinding, Int. J. Mach. Tool Des. 11 (1971) 223.
- [68] M.E. Riley, M.E. Coltran, D.J. Diestler, A velocity reset method of simulating thermal motion and damping in gas–solid collisions, J. Chem. Phys. 88 (9) (1988) 5934.
- [69] L.M. Raff, D.L. Thompson, The classical trajectory approach to reactive scattering,, in: Theory of Chemical Reaction Dynamics III CRC Press, 1985, Chapter I.
- [70] L.M. Raff, Theoretical investigations of chemical and physical processes under matrix isolation conditions, in: D.L. Thompson (Ed.), Modern Methods for Multidimensional Dynamics Computations in Chemistry, World Scientific Publishing, NJ, 1998, pp. 266–354.